UNIVERSITY OF CALGARY

Complete Temporal Characterization of Single Photons

by

Adarsh Shankar Prasad

A THESIS

SUBMITTED TO THE FACULTY OF GRADUATE STUDIES

IN PARTIAL FULFILLMENT OF THE REQUIREMENTS FOR THE

DEGREE OF MASTER OF SCIENCE

DEPARTMENT OF PHYSICS AND ASTRONOMY

CALGARY, ALBERTA

SEPTEMBER, 2014

Abstract

Precise information about the temporal mode of optical states is crucial for optimizing their interaction efficiency between themselves and/or with matter in various quantum communication devices. Here we propose and experimentally demonstrate a method of determining both the real and imaginary components of a single photon's temporal density matrix by measuring the autocorrelation function of the photocurrent from a balanced homodyne detector at multiple local oscillator frequencies. We lay the theoretical foundation for our work and describe the experimental methods involved in detail. We show the results of testing our method on single photons heralded from bi-photons generated via four-wave mixing in an atomic vapor. We develop an appropriate theoretical model for our experimental settings and describe the involved calculations explicitly. The obtained experimental results show excellent agreement with theoretical predictions for the various settings involved.

Acknowledgements

I wish to utilize this opportunity to thank all those people without who going through graduate school would have been impossible.

First and foremost, I would like to thank my supervisor Prof. Alex Lvovsky for being a very understanding and supporting mentor as well as for being such a good teacher. His constant interaction with me with regards to "progress in research" was extremely helpful in finishing my masters on time. I would like to thank him for guiding me through extremely difficult phases of grad school life which at times has been overwhelming.

Secondly, I would like to thank my colleagues with who I worked during the course of two years. In no particular order, I would like to thank Yuri, Travis and Zhongzhong for bearing with my over competitive nature and for having useful discussions which has been my major source of learning.

I would like to thank other colleagues of my research group in no particular order for helping me in any way in my masters: Aveek, Di, Eugene, Arina, Daniel, Kenzo, Andrew, Ryan, Pan, Connor, Tayebe, Arturo, Andal. Please excuse me if I forgot to include someone's name.

Apart from all of the above, I would like to thank other colleagues from the *Institute for Quantum Science and Technology* and from Department of Physics in general for being supportive friends. In no particular order again, I would like to thank my friends- Randy, Hon-wai, Tian, Sofie, Mojtaba, Mahdi, Adams, Abhirup, Sourabh, Erhan, Hassan, Mark, Varun, Behzad, Chris, Marcelo, Roya, Anna, Ambrish, Eliot and any other person whose has been a friend to me.

In the end, but not the least I would like to thank my family for being supportive throughout.

Table of Contents

List of Tables

List of Figures and Illustrations

List of Symbols, Abbreviations and Nomenclature

Symbol	Definition
A.U.	Arbitrary units
AOM	Acousto-optic modulator
BS	Beam splitter
c.c.	Complex conjugate
CW	Continuous wave
em	electromagnetic
EOM	Electro-optic modulator
FSR	Free spectral range
FWM	Four-wave mixing
HWP	Half wave plate
LO	Local oscillator
ns	Nanoseconds
PBS	Polarizing beam splitter
POHT	Polychromatic optical heterodyne tomography
QWP	Quarter wave plate
SMF	Single mode fiber
SPCM	Single photon counting module
TDM	Temporal density matrix
TE	Transverse electric
TMF	Temporal mode function

Chapter 1

Introduction

In this thesis, I discuss the technique of *polychromatic optical heterodyne tomography* (POHT), developed and implemented by us as a means to characterize a single photon completely in the time domain. This experimental technique enables one to calculate the temporal density matrix of a single photon, from which any complex temporal mode structure can be determined with certainty. The dependence of single photon related measurements on the temporal mode of the photon will be elucidated later in this section and in chapter 2. In general, single photons and single photon qubits are key ingredients of most quantum optical experiments such as quantum cryptography [2], quantum teleportation [3], quantum repeaters [4] and quantum computing [5]. The spatio-temporal mode of those single photons, and in general of any complex photonic states [6, 7, 8], depends on the experimental configuration including the characteristics of the generation process [9, 10, 11]. However, the target application experimental setup may require the single photon states to have a well-defined modal structure [12] as imperfect mode matching can introduce inefficiencies into the system [13, 14]. In particular, generation of single photons with a desired temporal structure and its temporal characterization is of wide interest to research communities implementing light matter interaction at the single photon level [15, 16, 17].

Having knowledge of the modal structure is crucial for making measurements on states having a temporal mode function (TMF) $\phi(t)$, with a corresponding annihilation operator in this mode defined as

$$\hat{A} = \int_{-\infty}^{\infty} \hat{a}_t \phi(t) dt, \tag{1.1}$$

where $\hat{a}_t$ represents the instantaneous annihilation operator at time t. For example, homodyne detection of single photon states using a continuous wave local oscillator (LO) requires

knowledge of the temporal mode to accurately calculate the quadratures as discussed in [18]. Alternatively in pulsed regime, the temporal mode of the LO is matched to the mode of the single photon, using either *a priori* knowledge of the single photon temporal mode or by ensuring that both are prepared identically [19]. An approximate guess of such temporal mode can be inferred theoretically based upon the bandwidth of any filtering cavities [20] or in the case of pulses by that of the sources such as pulsed pump lasers. However, the observed temporal mode may also be affected by experimental imperfections such as birefringence in the optics, non-ideal detector response functions, and imperfections in either the cavity or the laser spectra. Hence, precise theoretical modeling of the temporal mode requires detailed knowledge of the experimental setup. Furthermore, such methods still cannot work for unknown temporal modes that have perhaps been sent in by a third party in a communications scheme. To this end, an experimental technique for precise temporal characterization of single photons in any arbitrary temporal mode would be a valuable tool. While techniques have been developed for determining the spatial mode of single photons [21, 22], extension of the same into temporal domain is a challenging task.

Several techniques have been proposed and used for determination of the TMF $\phi(t)$ for single photons. One of the simplest techniques enables determination of the probability of photon detection $|\phi(t)|^2$ as a function of time using counting statistics [23]. However, such a technique loses any phase information about the temporal mode. A technique which overcame this problem uses adaptive waveform shaping of the homodyne LO pulses [24], which heuristically finds the LO temporal mode that maximizes the single photon efficiency. This occurs when the LO temporal mode matches the signal photon temporal mode, enabling measurement of $\phi(t)$. However, such precise pulse shaping is quite sophisticated experimentally, in particular for ultrashort pulses and cannot be extended to the continuous wave regime. Furthermore, this technique has been demonstrated only for pure temporal modes.

If the photons are wider than ultrashort pulses or, in other words, if the detection elec-

tronics is able to resolve the single photon measurements, the time-resolved statistics of a homodyne detector's output photocurrent can be analyzed. To this effect, MacRae *et. al* showed that the autocorrelation matrix corresponding to the homodyne photocurrent output can help estimate the real part of the temporal density matrix (TDM) defining the photon's temporal mode. This approach has subsequently been utilized for a Schrödinger cat state and two photon Fock states [25]. However, this technique still lacks the ability to extract the imaginary part of the TDM because the autocorrelation matrix did not have any dependence on the imaginary part of the TDM owing to zero detuning of LO with respect to the signal.

Our technique, the details of which is the core of my thesis, allows us to extract both the real and imaginary part of the TMF. In particular, we characterize the single photon completely in the time domain by determining its complete complex TDM. Our method allows us to characterize both pure and mixed temporal modes. We call our technique *polychromatic optical heterodyne tomography*. The words chosen can be explained as follows. It is called *Polychromatic* because it uses multiple colors for the LO beam. We analyze the beat signal at the output of the homodyne detector which contains the encoded information about the TDM. This technique of mixing two spectrally offset optical signals to extract information about one of them is the main principle behind the technique of optical heterodyning. We reconstruct the temporal state (for pure modes) or the TDM (mixed state) from the heterodyne data, hence, the word tomography. The thesis is organized as follows:

In chapter 2, we discuss the basics of quantum optics. We start with explaining the quantization of light from where we jump to the quantum states of light. We describe Fock states, coherent states and squeezed states of light. We then describe how we are able to generate squeezed states of light in our laboratory using the technique of four-wave mixing. We then discuss about homodyne detectors and their usage in making measurements on quantum states of light. From there we arrive at the concept of temporal modes and provide the motivation for acquiring its knowledge.

In chapter 3, we introduce our technique of POHT. We lay its theoretical foundations. Following that we provide the details about the experimental setup and of performing the experiment.

In chapter 4, we show our experimental results. We calculate the theoretically expected temporal mode function (TMF) and temporal density matrix (TDM) for the various settings using the knowledge of our experimental setup. We demonstrate the agreement of the experimental observation with the theoretical predictions. Having obtained the temporal mode structure, we are able to calculate precisely the single photon efficiency for our experimental setup by finding out the fock basis density matrix of photon in Fock-basis.

Chapter 5, discusses the importance of our experimental technique along with its shortcomings, possible solutions to them and its applications in the future.

Chapter 2

Basics of Quantum Optics

2.1 Quantum Theory of Light

The exact nature of light had been a subject of debate for physicists. Sir Issac Newton's proposed in his treatise *Opticks* that light is made up of little particles which obey the same laws of physics as other masses and are so tiny that the particles in two beams intersecting each other do not scatter off each other. This was called the *Corpuscular theory of light*. On the other hand, the wave theory of light proposed by Huygens claimed that every point on a wave-front may be considered as a source of secondary wavelets which spread out in the forward direction at the speed of light. This was further championed by the discovery of interference of light in 1801 by Thomas Young in his famous experiment popularly known as the *Young's double-slit experiment* which could not be explained by particle theory of light. Sir James Clerk Maxwell's electromagnetic (*em*) theory of light illustrated beautifully how light can be understood as wave-like disturbances propagating through space. It was not until the twentieth century that the quantum picture of light started emerging.

Max Planck introduced the concept of quantization of light for the first time in his theory of blackbody radiation [26]. Albert Einstein's theory of photoelectric effect treated light as particles. Dirac's seminal paper on *the quantum theory of light* [27] was the first formal approach to quantizing the light and interpreting the consequences. In this section, we will review some basic formalism of the quantum theory of light.

2.1.1 Quantization of light

2.1.1.1 Energy of electromagnetic field

The quantization of *em* field aims at describing light similar to a quantum harmonic oscillator. To do so lets start from the solution of Maxwell's equation which represents the spatio-temporal mode of light. For a standing *em* field confined in a box of volume $V = L_x \times L_y \times L_z$, the Fourier series decomposition of the electric and magnetic field can be expressed as

$$\vec{E}(\vec{r},t) = \sum_{\vec{k},s} e^{i\vec{k}\cdot\vec{r}}\vec{u}_{\vec{k},s}(t) + c.c. \tag{2.1}$$

$$\vec{B}(\vec{r},t) = \sum_{\vec{k},s} e^{i\vec{k}\cdot\vec{r}}\vec{w}_{\vec{k},s}(t) + c.c. \tag{2.2}$$

The index s represents the one of the two possible orthogonal polarizations and $\vec{u}_{\vec{k},s}(t)$ and $\vec{w}_{\vec{k},s}(t)$ represent the time-dependent amplitudes of the electric and magnetic field. The index $\vec{k}$ is the wavevector for the plane *em* wave mode. Due to the boundary conditions for standing waves in the box, the wavevectors are discretized as $\vec{k} = (2\pi n_x/L_x, 2\pi n_y/L_y, 2\pi n_z/L_z)$ where $\{n_x, n_y, n_z\} \in \mathbb{N}$. The electric field and the magnetic field are perpendicular to each other satisfying the criterion: $\vec{B} = (\vec{k} \times \vec{E})/\omega$, ω being the angular frequency corresponding to the allowed wavevectors. The total energy for the field represented by Eq. (2.1) can be found for free space as

$$\begin{aligned} E_{tot} &= \frac{1}{2}(\epsilon_0 E^2 + \frac{B^2}{\mu_0}) \\ &= 2\epsilon_0 V \sum_{\vec{k},s} |\vec{u}_{\vec{k},s}(t)|^2 \end{aligned} \tag{2.3}$$

The above expression shows that the total energy of the *em* field is the sum of the energies in the individual modes. An important implication of this result is that propagation of one mode is unaffected by the other modes and that they can be treated separately. Here, we will show the quantization of one of the modes represented by $\vec{k}, s$ with the same treatment

applicable to all other modes. Eq. (2.3) for a single mode can be rewritten as

$$H_{\vec{k},s} = 2\epsilon_0 V u^*_{\vec{k},s}(t) u_{\vec{k},s}(t) \tag{2.4}$$

where H stands for the Hamiltonian of the mode defined by $\{\vec{k}, s\}$.

2.1.1.2 Transition from Classical to Quantum

Let us introduce the following transformations

$$X_{\vec{k},s}(t) = \sqrt{\frac{2\epsilon_0 V}{\hbar\omega}} \frac{u_{\vec{k},s}(t) + u^*_{\vec{k},s}(t)}{\sqrt{2}} \tag{2.5a}$$

$$P_{\vec{k},s}(t) = \sqrt{\frac{2\epsilon_0 V}{\hbar\omega}} \frac{u_{\vec{k},s}(t) - u^*_{\vec{k},s}(t)}{\sqrt{2i}} \tag{2.5b}$$

Substituting $u_{\vec{k},s}$ from Eq. (2.5) in Eq. (2.4), one can easily show that the Hamiltonian for a single mode can be expressed as

$$H_{\vec{k},s} = \frac{\hbar\omega}{2} \left[X^2_{\vec{k},s}(t) + P^2_{\vec{k},s}(t) \right] \tag{2.6}$$

The expression for the Hamiltonian of a single mode resembles that of a classical harmonic oscillator[1]. In classical mechanics, the phase space variables obey the *canonical equations of motion*

$$\dot{p} = -\frac{\partial H}{\partial x} \tag{2.8a}$$

$$\dot{x} = \frac{\partial H}{\partial p} \tag{2.8b}$$

In quantum mechanics, the canonical equations of motion for the position and momentum can be written as

$$\dot{P}_{\vec{k},s} = -\frac{1}{\hbar} \frac{\partial H}{\partial X_{\vec{k},s}} \tag{2.9a}$$

$$\dot{X}_{\vec{k},s} = \frac{1}{\hbar} \frac{\partial H}{\partial P_{\vec{k},s}} \tag{2.9b}$$

[1]The classical Hamiltonian is given as [28]

$$H = \frac{1}{2m} \left(p^2 + m^2\omega^2 x^2 \right) \equiv E, \tag{2.7}$$

where x, p represent position and momentum of a harmonically oscillating particle of mass m with frequency and energy ω, E

The factor of $\hbar$ comes from the way the phase space variables are defined in quantum mechanics, namely, $X = x/\hbar, P = p/\hbar$. We shall assume $\hbar$ equal one for simplicity. Additionally, the *Poissonian bracket* in classical mechanics translates into a commutator as

$$[\hat{X}_{\vec{k},s}, \hat{P}_{\vec{k},s}] = i \tag{2.10}$$

These quantum mechanical operators $\hat{X}$ and $\hat{P}$ have the corresponding eigenstates as $|X\rangle$ and $|P\rangle$ respectively, such that following hold

$$\hat{X}_{\vec{k},s} |X_{\vec{k},s}\rangle = X_{\vec{k},s} |X_{\vec{k},s}\rangle \tag{2.11a}$$

$$\hat{P}_{\vec{k},s} |P_{\vec{k},s}\rangle = P_{\vec{k},s} |P_{\vec{k},s}\rangle \tag{2.11b}$$

and the orthogonality exists as [2]

$$\left\langle X_{\vec{k},s} \middle| X'_{\vec{k},s} \right\rangle = \delta(X_{\vec{k},s} - X'_{\vec{k},s}) \tag{2.12a}$$

$$\left\langle P_{\vec{k},s} \middle| P'_{\vec{k},s} \right\rangle = \delta(P_{\vec{k},s} - P'_{\vec{k},s}) \tag{2.12b}$$

The position and momentum eigenstates are related to each other by the *de Broglie wave*:

$$\langle X_{\vec{k},s} | P_{\vec{k},s} \rangle = \frac{1}{\sqrt{2\pi}} e^{i P_{\vec{k},s} X_{\vec{k},s}} \tag{2.13}$$

Therefore, for any arbitrary state $|\psi\rangle$

$$\langle X|\psi\rangle = \frac{1}{\sqrt{2\pi}} \int_{-\infty}^{\infty} \langle P|\psi\rangle \, e^{iPX} dP \tag{2.14a}$$

$$\langle P|\psi\rangle = \frac{1}{\sqrt{2\pi}} \int_{-\infty}^{\infty} \langle X|\psi\rangle \, e^{-iPX} dX \tag{2.14b}$$

Eq. (2.14) also signifies that the wavefunction in the position and momentum bases are Fourier transform of each other. Using the above two equations one can find two useful expressions which we would use later in determining the position space wavefunction of the

[2] Because these states are not normalizable, they, strictly speaking belong not to the Hilbert space, but to the so-called *rigged Hilbert space*. See R. de la Madrid, Eur. J. Phys. 26, 287-312 (2005) for details.

Fock-states

$$\langle X|\hat{P}|\psi\rangle = -i\frac{d}{dX}\psi(X) \tag{2.15a}$$

$$\langle P|\hat{X}|\psi\rangle = i\frac{d}{dP}\psi(P) \tag{2.15b}$$

2.1.1.3 Creation and Annihilation operators

The annihilation operator for a temporal mode is defined as

$$\hat{a}_{\vec{k},s} = \frac{\hat{X}_{\vec{k},s} + i\hat{P}_{\vec{k},s}}{\sqrt{2}} \tag{2.16}$$

Corresponding to it, the creation operator can be defined as

$$\hat{a}^{\dagger}_{\vec{k},s} = \frac{\hat{X}_{\vec{k},s} - i\hat{P}_{\vec{k},s}}{\sqrt{2}} \tag{2.17}$$

Following commutation relation exists

$$[\hat{a}_{\vec{k},s}, \hat{a}^{\dagger}_{\vec{k'},s'}] = \delta_{\vec{k},\vec{k'}}\delta_{s,s'} \tag{2.18}$$

The *Kronecker-delta*[3] function comes from the fact that individual modes represented by the wavevector and polarization index $\vec{k}, s$ are independent of each other as discussed in Section 2.1.1.1. The Hamiltonian for a single mode $\{\vec{k}, s\}$ can then be represented as

$$\hat{H}_{\vec{k},s} = \hbar\omega\left(\hat{a}^{\dagger}_{\vec{k},s}\hat{a}_{\vec{k},s} + \frac{1}{2}\right) \tag{2.19}$$

The operator $\hat{a}^{\dagger}_{\vec{k},s}\hat{a}_{\vec{k},s}$ is called the number operator represented by $\hat{n}_{\vec{k},s}$ defined in Eq. (2.21).

2.1.1.4 Fock states

Fock states represented by $|n_{\vec{k},s}\rangle$ are the eigenstates of the Hamiltonian operator defined by (2.19). Since the number operator $\hat{n}_{\vec{k},s}$ and the Hamiltonian $\hat{H}_{\vec{k},s}$ commute with each other,

[3]Kronecker delta function is defined as:

$$\delta_{ij} = \begin{cases} 1, & \text{if } i = j, \\ 0, & \text{if } i \neq j. \end{cases}$$

therefore, Fock states are also eigenstates of the former. The eigenvalue equations can be written as

$$\hat{H}_{\vec{k},s}\,|n_{\vec{k},s}\rangle = \hbar\omega\left(n_{\vec{k},s}+\frac{1}{2}\right) \tag{2.20}$$

$$\hat{n}_{\vec{k},s}\,|n_{\vec{k},s}\rangle = n_{\vec{k},s}\,|n_{\vec{k},s}\rangle \tag{2.21}$$

Eq. (2.21) can further be used along with the commutation relation given by Eq. (2.18) to arrive at the following important relations

$$\hat{a}_{\vec{k},s}\,|n_{\vec{k},s}\rangle = \sqrt{n_{\vec{k},s}}\,|n_{\vec{k},s}-1\rangle \tag{2.22}$$

$$\hat{a}^{\dagger}_{\vec{k},s}\,|n_{\vec{k},s}\rangle = \sqrt{n_{\vec{k},s}+1}\,|n_{\vec{k},s}+1\rangle \tag{2.23}$$

$$\hat{a}^{\dagger}_{\vec{k},s}\,|0_{\vec{k},s}\rangle = 0 \tag{2.24}$$

The eigenvalues of the number operator must be a must be a *nonnegative* integer. The reason for this is that energy of an *em-field* can never be negative. Eq (2.20) allows the minimum energy of an *em-field* to be $\frac{1}{2}\hbar\omega$ (also called *zero-point energy*) which corresponds to the lowest energy Fock state that exists, $|0\rangle$, called the vacuum state. There are several evidences for the existence of such a state such as spontaneous emission in atoms, lamb shift and quantum beats which have been discussed in details in reference [29]. A higher energy state state can be obtained from the vacuum state by [4]

$$|n_{\vec{k},s}\rangle = \frac{\left(\hat{a}^{\dagger}_{\vec{k},s}\right)^{n}}{\sqrt{n!}}\,|0_{\vec{k},s}\rangle \tag{2.25}$$

Each consecutive number state is separated in energy by a value $\hbar\omega$ which is a direct implication of quantization of energy of light. The quantum state of light for mode $\vec{k},s$ could be any possible superposition of the Fock states of that mode as

$$|\Psi_{\vec{k},s}\rangle = \sum_{n_{\vec{k},s}} c_{n_{\vec{k},s}}\,|n_{\vec{k},s}\rangle \tag{2.26}$$

[4]The vacuum state on the right hand side of Eq. (2.25) can be written without the subscript $\vec{k},s$. However, the annihilation operator for mode $\vec{k},s$ will only excite vacuum state corresponding to mode $\vec{k},s$ to $|1_{\vec{k},s}\rangle$.

where, $c_{n_{\vec{k},s}}$ are the probability amplitudes. One can find the wavefunction of the Fock states using Eq. (2.15), (2.16), (2.24), (2.25) in position space as

$$\psi_n(X) = \frac{H_n(X)}{\pi^{1/4}\sqrt{2^n n!}} e^{-X^2/2} \tag{2.27}$$

where $H_n(X)$ are the Hermite polynomials.

In this section, we have been using a specific mode $\vec{k}, s$. We shall drop this convention from now on for the sake of clarity unless otherwise we need to be specific about the mode of a state. In the coming subsection, we shall discuss about a very important quantum state which comes as a result of a special type of superposition of the Fock states, called *coherent states of light*.

2.1.1.5 Coherent states

A coherent state $|\alpha\rangle$ is an eigenstate of the annihilation operator with an eigenvalue α (called the coherent state amplitude):

$$\hat{a}\,|\alpha\rangle = \alpha\,|\alpha\rangle \tag{2.28}$$

where α is a complex number. The coherent state can be decomposed in the Fock basis as

$$|\alpha\rangle = \sum_{n=0}^{\infty} \frac{\exp(|\alpha|^2/2)\alpha^n}{\sqrt{n!}}\,|n\rangle \tag{2.29}$$

Consequently, the photon number distribution for a coherent state is *Poissonian*. In other words, if one performs energy measurement on the coherent, the probability to project it onto a particular Fock state is given by

$$\mathrm{pr}_n = |\,\langle n|\alpha\rangle\,|^2 = e^{-|\alpha|^2}\frac{|\alpha|^{2n}}{n!} \tag{2.30}$$

A field in coherent state is a minimum uncertainty state with equal uncertainties in the two quadrature components $\hat{X}$ and $\hat{P}$. Evolution of coherent state with time can be obtained by action of the evolution operator $e^{-i\hat{H}t/\hbar}$ on the coherent state as

$$e^{-i\hat{H}t/\hbar}\,|\alpha\rangle = e^{-i\omega t/2}\,|\alpha e^{-i\omega t}\rangle \tag{2.31}$$

This can be interpreted as the initial coherent state $|\alpha\rangle$ evolving into a different coherent state $|\alpha e^{-i\omega t}\rangle$ with time. This corresponds to an clockwise rotation of initial coherent state with an angular frequency ω in the $X - P$ phase space, where ω is the frequency mode corresponding to the Hamiltonian $\hat{H}$ in Eq. (2.31) under which the coherent state evolves.

2.1.2 Phase space probability distributions

Phase space density is a concept often encountered in classical and statistical mechanics. To understand it intuitively one can imagine an ensemble of particles. Suppose that there is a classical 2D system represented in the space of its canonical variables $x,\ p$ with a certain distribution of the particles. The probability that a particle chosen at random has certain values of x and p resembles closely to what we are going to define as Wigner function in the quantum domain. For the sake of understanding, let us assume that $w(x, p)$ represents such a classical probability distribution.

Let us consider a classical observable defined as

$$x_\theta \equiv x\cos\theta + p\sin\theta \tag{2.32}$$

where θ is the angle made with the x-axis in the phase space. If we make several measurements for this observable, the resulting histogram of the recorded data is called the *marginal distribution* $\mathrm{pr}(x_\theta)$. This marginal distribution is the integral projection of the phase space probability function on a vertical plane oriented at an angle θ with respect to the x axis as

$$\mathrm{pr}(x_\theta) = \int_{-\infty}^{\infty} w(x\cos\theta - p\sin\theta, x\sin\theta + p\cos\theta)dp \tag{2.33}$$

2.1.2.1 Wigner function

For the quantum case, we just need to replace the classical variables x, p with their quantum counterparts. The quadrature observable is now defined as

$$\begin{aligned} \hat{X}_\theta &\equiv \hat{X}\cos\theta + \hat{P}\sin\theta \\ &= \frac{\hat{a}^\dagger e^{i\theta} + \hat{a}e^{-i\theta}}{\sqrt{2}} \end{aligned} \tag{2.34}$$

The marginal distribution for a quantum state with a density matrix $\hat{\rho}$ is defined as

$$\mathrm{pr}(\hat{X}_\theta) = \mathrm{Tr}(\hat{\rho}\hat{X}_\theta) \tag{2.35}$$

In quantum mechanics, Heisenberg's uncertainty principle prevents one from knowing the position and momentum of a particle simultaneously. Quantum mechanics also allows the probability to be negative which is not possible classically. For this reason, Wigner function is quantum mechanics is called a *quasiprobability distribution* in the phase space and is represented by $W(X, P)$. For a state with a density matrix $\hat{\rho}$, the Wigner function is defined as

$$W_{\hat{\rho}}(X, P) = \frac{1}{2\pi}\int_{-\infty}^{+\infty} e^{iPQ}\left\langle X - \frac{Q}{2}\right|\hat{\rho}\left|X + \frac{Q}{2}\right\rangle dQ \tag{2.36}$$

Wigner function satisfies two important properties of normalization and linearity.

$$\iint_{-\infty}^{+\infty} W_{\hat{\rho}}(X, P)dXdP = 1 \tag{2.37}$$

$$W_{\alpha\hat{\rho}_1+\beta\hat{\rho}_2}(X, P) = \alpha W_{\hat{\rho}_1}(X, P) + \beta W_{\hat{\rho}_2}(X, P) \tag{2.38}$$

In general, Wigner function can also be defined for quantum operators ($\hat{O}$) similar to Eq. (2.36) which defined it for a density operator($\hat{\rho}$) corresponding to a quantum state. If $\hat{A}$ and $\hat{B}$ are two operators, Wigner function satisfies the following property

$$\mathrm{Tr}(\hat{A}\hat{B}) = 2\pi\iint_{-\infty}^{+\infty} W_{\hat{A}}(X, P)W_{\hat{B}}(X, P)dXdP \tag{2.39}$$

If we substitute $\hat{B} = |m\rangle\langle n|$, Eq. (2.39) can be used for determining the Fock state density matrix from a given Wigner function.

$$W_{\hat{\rho}}(X, P) = \iint_{-\infty}^{+\infty} P_{\hat{\rho}}(X', P')W_{|0\rangle\langle 0|}(X' - X, P' - P)dX'dP' \tag{2.40}$$

2.2 Optical Quantum State Engineering

2.2.1 Squeezed light

2.2.1.1 Squeezing

In the section 2.1.2, we saw that any quantum state of light has some finite uncertainty in the quadratures which makes the Wigner function of the quantum state spread out in the phase space. It is a consequence of the Heisenberg's uncertainty principle which states that there is always some uncertainty associated with the product of the two observables given by

$$\Delta X \Delta P \geq \frac{1}{2} \tag{2.41}$$

Coherent states have an uncertainty as close to a classical state as quantum mechanics allows. For this reason it is often called the minimum uncertainty state. Because coherent states are displaced vacuum states, it has the same uncertainty in position and momentum quadrature as the vacuum state, product being equal to the minimum allowed by the Heisenberg's uncertainty principle (see Eq. (2.41)). Squeezed light in quantum optics can show even lower uncertainty in one of the quadratures but at the cost of increased uncertainty along the conjugate quadrature.

2.2.1.2 Single mode squeezed light

The squeezing operator for a single spatio-temporal mode can be represented as

$$\hat{S}(\zeta) = \exp[-i\zeta(\hat{a}^2 - \hat{a}^{\dagger 2})] \tag{2.42}$$

where, ζ is the squeezing parameter. For a physical system producing squeezed light, the squeezing parameter depends on the product of coupling strength and the interaction time system components. The effect of this operator on the quadratures is given as

$$\hat{X} \rightarrow \hat{X}e^{-\zeta} \tag{2.43}$$

$$\hat{P} \rightarrow \hat{P}e^{+\zeta} \tag{2.44}$$

2.2.2 Four-wave mixing (FWM)

2.2.2.1 Two-mode squeezing: Quantum treatment of Four-wave mixing

In our experimental system we use a nonlinear process known as *four-wave mixing* which will be discussed in the following section. Four-wave mixing in its simplest sense involves interaction of light in two spatio-temporal modes to generate a two-mode output state. This output state generated is called *two-mode squeezed state*. The two mode squeezing operator is given by

$$\hat{S}_2(\zeta) = \exp[-i\zeta(\hat{a}_1\hat{a}_2 - \hat{a}_1^\dagger\hat{a}_2^\dagger)] \tag{2.45}$$

The squeezing generated by such an operator is results in following transformations

$$\hat{a}_1 \rightarrow \hat{a}_1\cosh\zeta - \hat{a}_2^\dagger\sinh\zeta; \tag{2.46}$$

$$\hat{a}_2 \rightarrow \hat{a}_2\cosh\zeta - \hat{a}_1^\dagger\sinh\zeta; \tag{2.47}$$

$$\hat{X}_1 \pm \hat{X}_2 \rightarrow (\hat{X}_1 \pm \hat{X}_2)e^{\mp\zeta}; \tag{2.48}$$

$$\hat{P}_1 \pm \hat{P}_2 \rightarrow (\hat{P}_1 \pm \hat{P}_2)e^{\pm\zeta}; \tag{2.49}$$

2.2.2.2 Classical treatment of FWM in atomic vapor

Four-wave mixing in an atomic vapor produces highly multimode (frequency and spatial) quantum-correlated twin beams which display continuous variable entanglement such that for a given pair of spatio-temporal modes the quantum fluctuations in one mode cannot be described independently of the other mode. We use Rubidium 85 vapor as the atomic gain medium which exhibits $\chi^{(3)}$ nonlinearity when the phase matching conditions are met. In this section, we shall see some of the aspect of the process in detail.

A nonlinear interaction in achieved in a medium because of its response to external electric field in the form of induced polarization. In general the response of materials to an

applied electric field $\vec{E}$ can be expressed as

$$\begin{aligned}\vec{P}(t) &= \epsilon_0 \frac{1}{2\pi} \int_{-\infty}^{+\infty} \chi^{(1)}(\tau)\vec{E}(t-\tau)d\tau \\ &+\epsilon_0 \frac{1}{(2\pi)^2} \iint_{-\infty}^{+\infty} \chi^{(2)}(\tau_1,\tau_2)\vec{E}(t-\tau_1)\vec{E}(t-\tau_2)d\tau_1 d\tau_2 \\ &+\epsilon_0 \frac{1}{(2\pi)^3} \iiint_{-\infty}^{+\infty} \chi^{(3)}(\tau_1,\tau_2,\tau_3)\vec{E}(t-\tau_1)\vec{E}(t-\tau_2)\vec{E}(t-\tau_3)d\tau_1 d\tau_2 d\tau_3 \\ &+\ldots \end{aligned} \tag{2.50}$$

where $\chi^{(n)}$ represents nonlinear electric susceptibility tensor of order n [30]. Spontaneous parametric down-conversion [31] and four-wave mixing [32] are two processes which show a high nonlinear response because of $\chi^{(2)}$ and $\chi^{(3)}$ susceptibility We can rewrite the above expression in the frequency domain as

$$\begin{aligned}\vec{P}(\omega) &= \epsilon_0 \chi^{(1)}(\omega)\vec{E}(\omega) \\ &+\epsilon_0 \iint_{-\infty}^{+\infty} \chi^{(2)}(\omega_1,\omega_2)\delta(\omega-\omega_1-\omega_2)\vec{E}(\omega_1)\vec{E}(\omega_2)d\omega_1 d\omega_2 \\ &\epsilon_0 \iiint_{-\infty}^{+\infty} \chi^{(3)}(\omega_1,\omega_2,\omega_3)\delta(\omega-\omega_1-\omega_2-\omega_3)\vec{E}(\omega_1)\vec{E}(\omega_2)\vec{E}(\omega_3)d\omega_1 d\omega_2 d\omega_3 \\ &\ldots \end{aligned} \tag{2.51}$$

The *delta function* in the Eq. (2.51) shows that the frequency of the induced polarization is the sum of all the possible (both negative and positive) frequencies of the applied electric fields. In the case of atomic vapor like in our system, the first order susceptibility is vanishingly small and the second order susceptibility vanishes due to its isotropicity [30]. Therefore, the three frequency modes interact with each other with the help of 3$^{\text{rd}}$ order susceptibility as:

$$\vec{P}_i^{NL}(\omega) = \epsilon_0 \sum_{ijkl} \chi_{ijkl}^{(3)}(\omega_1,\omega_2,\omega_3)\delta(\omega-\omega_1-\omega_2-\omega_3)\vec{E}_j(\omega_1)\vec{E}_k(\omega_2)\vec{E}_l(\omega_3)d\omega_1 d\omega_2 d\omega_3, \tag{2.52}$$

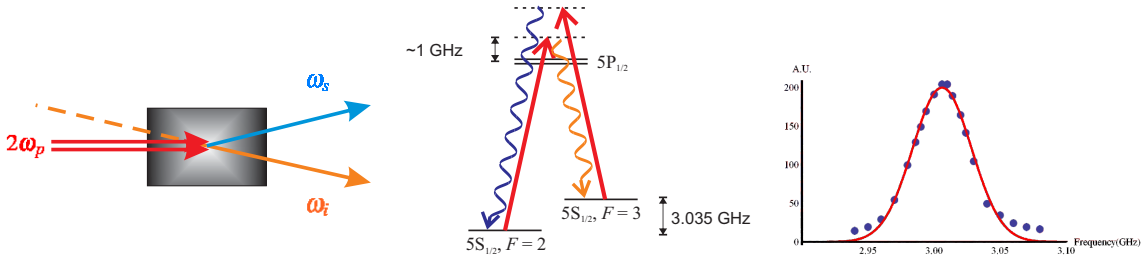

(a) (b) (c)

Figure 2.1: (a) FWM mechanism: Two pump photons of frequency (ω_p, red) interact to generate one photon of idler (ω_i, orange) and one photon of signal (ω_s, blue). The output beams are at certain angle (not necessarily the same) to the incident pump beam. The dashed line shows the orientation of the seed beam being roughly in line with the idler beam for alignment purpose. (b) The ^{85}Rb three-level Λ system, with the fields' configuration shown. [1]. (c) The gain-profile of the FWM process with respect to the seed detuning.

The interaction mechanism in shown in the Fig. (2.1). Two identical pump photons (with wavevector $\vec{k_p}$, frequency ω_p) acts as the input and generate output beams: *idler* (wavevector $\vec{k_i}$, frequency ω_i) and its conjugate, *signal* (wavevector $\vec{k_s}$, frequency ω_s). Conservation of energy and momentum for this process gives the following relation.

$$2\omega_p = \omega_s + \omega_i \tag{2.53a}$$

$$2\vec{k_p} = \vec{k_s} + \vec{k_i} \tag{2.53b}$$

Assuming that the electric fields are slowly propagating and roughly collinear along direction (say z) [5], we can write total electric field at any point as

$$\vec{E}_m(\vec{r},t) = \vec{\mathcal{E}}_m(z)e^{i(\vec{k}_m z - \omega_m t)} + c.c., \qquad \text{where } m \in \{p,s,i\} \tag{2.54}$$

such that $\mathcal{E}(z)$ gives the slowly varying envelop amplitude along the propagation axis z. The three beams represented by Eq. (2.54) may interact with each other to generate 44 possible output frequencies for the induced polarization but only one combination[6] survives owing to

[5]The probe beam and its conjugate make a small angle with the pump such that the momentum conservation holds (See Eq. (2.53b)) but we can assume collinearity for simplicity

[6]It should be noted that FWM has a finite gain bandwidth and so will the output idler and the signal frequencies as long as they satisfy Eq. (2.53). However, out of the 81 components of $\chi^{(3)}$, only one component turns out to be effective which in turn restricts the frequency of the induced polarization according to Eq. (2.52).

the constraint posed by the tensor nature of the $\chi^{(3)}$ susceptibility and polarization direction of the interacting beams. Therefore, rewriting Eq. (2.52) using Eq. (2.54) and treating the electric field as scalars, we get

$$\vec{P}_i^{NL}(\omega_i) = \epsilon_0 \chi^{(3)} \mathcal{E}_p^2 \mathcal{E}_s^* e^{i(2k_p - k_s)z - (2\omega_p - \omega_s)t} = \epsilon_0 \chi^{(3)} \mathcal{E}_p^2 \mathcal{E}_s^* e^{i(2k_p - k_s)z - \omega_i t} \tag{2.55}$$

where the subscript stand for signal (s), idler (i) and pump (p) and $\chi^{(3)} \equiv \chi^{(3)}_{ipps}(\omega)$ To see the dynamics of the system we should solve the wave equation

$$(\nabla^2 - \partial_t^2)E = \frac{1}{c^2 \epsilon_0} \partial_t^2 P \tag{2.56}$$

under the assumptions of slowly varying amplitude[7] and paraxial wave approximations[8]. From Eq. (2.54),(2.55),(2.56), we get for the idler field

$$\partial_z \mathcal{E}_i = i\kappa \mathcal{E}_s^* e^{i\Delta k z} \tag{2.57}$$

where $\Delta k = 2k_p - k_i - k_s$ is defined as the phase mismatch parameter and $\kappa = \frac{k_i \chi^{(3)}}{2c\epsilon_0} \epsilon_0 c \mathcal{E}_p^2 = \frac{k_i \chi^{(3)}}{2c\epsilon_0} I_p$ is a constant depending upon the pump intensity I_p which is constant as a result of the assumption that the pump does not get depleted. The signal field is obtained similarly

$$\partial_z \mathcal{E}_s = i\kappa \mathcal{E}_i^* e^{i\Delta k z} \tag{2.58}$$

Assuming[9] $\Delta k \approx 0$ and Differentiating Eq. (2.57) and (2.58), we can arrive at the coupled differential equation

$$\partial_z \mathcal{E}_i = i\kappa \mathcal{E}_s^* \tag{2.59a}$$

$$\partial_z \mathcal{E}_s = i\kappa \mathcal{E}_i^* \tag{2.59b}$$

Solving the coupled differential equation 2.59 and implementing boundary conditions in terms of $\mathcal{E}_i(0)$ and $\mathcal{E}_s(0)$ we can obtain the following solution

$$\mathcal{E}_i(\zeta) = \mathcal{E}_i(0)\cosh(\zeta) + \mathcal{E}_s^*(0)\sinh(\zeta) \tag{2.60}$$

$$\mathcal{E}_s(\zeta) = \mathcal{E}_s(0)\cosh(\zeta) + \mathcal{E}_i^*(0)\sinh(\zeta) \tag{2.61}$$

[7] It states that the variation in the shape of the envelop in time and space occurs much slower than the period and wavelength respectively. Mathematically $\partial_z \mathcal{E} \ll k\mathcal{E}$ and $\partial_t \mathcal{E} \ll \omega \mathcal{E}$ and second derivatives vanish.

[8] $\partial_z^2 \mathcal{E} \ll 2ik\partial_z \mathcal{E}$

[9] In our system $\lambda_s \approx \lambda_i \approx \lambda_p$

where $\zeta \equiv |\kappa| z$. Replacing the electric field amplitudes by corresponding annihilation operators

$$\mathcal{E}_i(0) \rightarrow \hat{a}_i(0) \ , \tag{2.62a}$$

$$\mathcal{E}_s(0) \rightarrow \hat{a}_s(0) \ , \tag{2.62b}$$

$$\mathcal{E}_i(\zeta) \rightarrow \hat{a}_i \ , \tag{2.62c}$$

$$\mathcal{E}_s(\zeta) \rightarrow \hat{a}_s \ , \tag{2.62d}$$

we can retrieve the two-mode squeezing transformation given by Eqs. (2.46) and (2.47).

2.3 Detection of quantum light

2.3.1 Principle behind homodyne detection

Homodyne detection is a well known technique which is used to determine the field quadratures of an electromagnetic mode. A typical homodyne setup looks as shown in Fig. 2.2. The setup consists of a 50 : 50 beam splitter, the output spatial modes of which are incident on identical photodiodes. The output of the homodyne detector is the difference in the photocurrent of two photodiodes. One of the input modes is a high intensity CW classical beam called the *local oscillator* (LO) which is spatially mode matched with the signal beam (the other input mode) to be detected. The signal beam is allowed to fall on the other input port of the beam splitter. Division of amplitude takes place and the output mode consists of interfering LO and signal field. It turns out that the output of the homodyne is proportional to the electric field amplitude of the signal or quantum mechanically the quadrature of the signal field mode. The calculation for the same has been described below.

Let the two input modes to the 50:50 beam splitter (refer Fig. 2.2) be represented by annihilation operator $\hat{a}_1$ and $\hat{a}_2$. The output modes $\hat{a}_1'$ and $\hat{a}_2'$ are then given by the beam

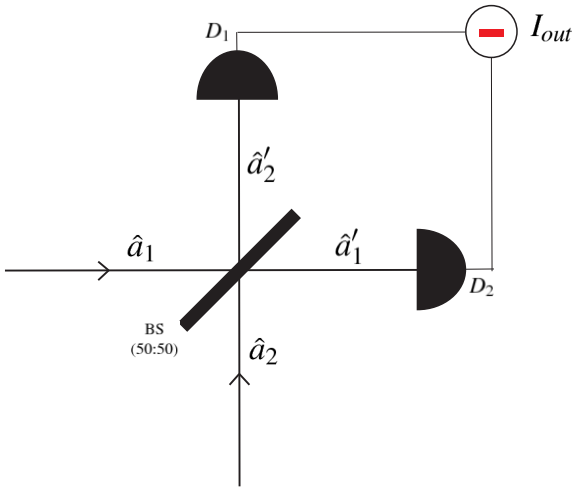

Figure 2.2: A typical homodyne detection setup: The two input modes $\hat{a}_1$ and $\hat{a}_2$ combine on a $50:50$ beam splitter (BS) to give the corresponding output modes $\hat{a}_1'$ and $\hat{a}_2'$ which are detected with pair matched photodiodes D1 and D2. The electronics of the detector subtract and amplify the difference of the photocurrent (I_{out}) generated by the two detectors to give an output voltage proportional to I_{out}.

splitter transformation as

$$\hat{a}_1' = (\hat{a}_1 - \hat{a}_2)/\sqrt{2} \tag{2.63}$$

$$\hat{a}_2' = (\hat{a}_1 + \hat{a}_2)/\sqrt{2} \tag{2.64}$$

The intensity of the two output modes are detected by the two photodiodes are proportional to the mean photon number in the two modes given by

$$\begin{aligned} I_{out}(t) &= A\,(\hat{n}_2' - \hat{n}_1') \\ &= A\left(\hat{a}_2'^{\dagger}\hat{a}_2' - \hat{a}_1'^{\dagger}\hat{a}_1'\right) \\ &= A\left(\hat{a}_1^{\dagger}\hat{a}_2 + \hat{a}_1\hat{a}_2^{\dagger}\right) \end{aligned} \tag{2.65}$$

Substituting one of the inputs as a coherent state with an optical phase $\theta' = \omega t + \theta_0$ and magnitude $|\alpha_{LO}|$ as $\hat{a}_2 = |\alpha_{LO}|e^{-i(\omega t+\theta_0)} = |\alpha|e^{-i\theta'}$ where the frequency ω corresponds to the frequency of the LO derived from an almost single-mode (in frequency) laser. It is important to mention this because if the signal happens to be of a different frequency (say ω_s), then the output photocurrent from the homodyne detector would have beats with a

frequency $\delta\omega = |\omega - \omega_s|$ which will be evident once we write the evolution of signal mode as $\hat{a}_1(t) = a_1 e^{-i\omega_s t}$ and substitute $\hat{a}_1$ and $\hat{a}_2$ into Eq. (2.65). In such a case, we obtain the homodyne output current to be

$$\begin{aligned} I_{out}(t) &= A|\alpha_{LO}| \left(\hat{a}_1^\dagger(t) e^{-i\theta} + \hat{a}_1(t) e^{i\theta}\right) \\ &= A|\alpha_{LO}| \left(\hat{a}_1^\dagger e^{-i(\delta\omega t + \theta_0)} + \hat{a}_1 e^{i(\delta\omega t + \theta_0)}\right) \end{aligned} \tag{2.66}$$

For our experiment we are not varying the initial phase of the LO θ_0. This phase can be varied for example by introducing a piezoelectric transducer mounted mirror in the LO beam path or even just by the temperature related air refractive index fluctuations. However, the time scale over which one data sample is recorded is usually too small to consider the effect of changes in refractive index or otherwise it cannot be neglected [33]. Therefore for simplicity we can assume $\theta_0 = 0$. We get

$$I_{out}(t) = A|\alpha_{LO}| \left(\hat{a}_1^\dagger e^{-i\theta} + \hat{a}_1 e^{i\theta}\right) \tag{2.67}$$

where $\theta = \delta\omega \cdot t$ is the relative optical phase. Comparing Eq. (2.67) with Eq. (2.34), we can easily see that Eq. (2.67) can be rewritten as

$$I_{out}(t) = 2^{1/2} A|\alpha_{LO}| \hat{X}_\theta(t) \tag{2.68}$$

where everything other than the quadrature $\hat{X}_\theta$ is constant.

2.3.2 Importance of temporal mode function (TMF) in measurements

Eq (2.68) represent the output photocurrent of the homodyne as a function of time. The annihilation operator in the right hand side of the equation imply that the quantum state of light being measured upon is in a temporal mode like a delta function. However, in actual experiments, the spatio-temporal mode function of single photons generated have a finite time-bandwidth depending upon the properties of the source. Therefore, the photon annihilation operator is a weighted superposition of the single mode annihilation operator

$\hat{a}_\omega$. This can be represented by[10]

$$\hat{A} = \int_{-\infty}^{+\infty} \tilde{\phi}(\omega)\hat{a}_\omega(0)d\omega \tag{2.69}$$

Since frequency and time space are Fourier images of each other, therefore, one can obtain Eq. (1.1) from Eq (2.69) by expressing $\tilde{\phi}(\omega)$ in the temporal basis as follows[11]

$$\begin{aligned}
\hat{A} &= \int_{-\infty}^{+\infty} \tilde{\phi}(\omega)\hat{a}_\omega(0)d\omega \\
&= \int_{-\infty}^{+\infty} \left[\int_{-\infty}^{+\infty} \phi(t)e^{-i\omega t}dt\right] \hat{a}_\omega(0)d\omega \\
&= \int_{-\infty}^{+\infty} \phi(t) \left[\int_{-\infty}^{+\infty} \hat{a}_\omega(0)e^{-i\omega t}d\omega\right] dt \\
&= \int_{-\infty}^{+\infty} \phi(t)\hat{a}_t dt
\end{aligned} \tag{2.70}$$

Since quadrature $\hat{X}_\theta(t)$ has one to one correspondence with the annihilation operator of the signal $\hat{a}_1$ (see Eq. (2.67)), therefore, the observed quadrature measurements corresponding to a broadband signal photon is obtained as an integration of the homodyne photocurrent over the TMF $\phi(t)$ of the signal photon as [18]

$$\begin{aligned}
\hat{Q}_{meas} &= \int \hat{X}_\theta(t)\phi(t)dt \\
&= C\int I_{out}(t)\phi(t)dt,
\end{aligned} \tag{2.71}$$

where, C is a constant equal to $\sqrt{2}A|\alpha_{LO}|$. The above way of determining the measured quadrature is valid only if the temporal mode $\phi(t)$ is real. In case of a complex temporal

[10]In Eq. (2.69), the annihilation operator for frequency mode ω is defined for an instance $t = 0$. Looking back in to literature (see chapter 10 of [34]), one can see that the notation of writing $\hat{a}_\omega(t = 0)$ is the correct notation. But the time is generally ignored unless there is any kind of time evolution to be taken care of as in atom-photon interaction (See [35]).

[11]$\hat{a}_t$ must not be confused with the $\hat{a}_\omega(t) = a_\omega(0)e^{-i\omega t}$. The latter is a single mode annihilation operator in the Heisenberg's picture, whereas the former is an annihilation operator like a delta function in time i.e., with infinite uncertainty in the frequency as opposed to former.

mode, we will have to substitute the actual annihilation operator $\hat{A}$ from Eq. (2.70) instead of $\hat{a}_1(t)$ into the expression for the homodyne current output given by Eq. (2.67) to get the observed quadrature as

$$\hat{Q}_{actual} = C' \int \phi^*(t)\ \hat{a}_t^\dagger\ e^{-i\theta}\ dt + c.c. \tag{2.72}$$

Eq. (2.71) and (2.72) have excluded the dependence of the measured quadrature on the temporal mode of the LO in the sense that the LO is assumed to be CW. In case the LO is pulsed, then the quadrature corresponding to the signal will be measured in a temporal mode which is the product of the temporal mode of the LO and that of the signal. This dependence can be easily observed if one substitutes operator $\hat{a}_2$ corresponding to the LO mode as $\hat{a}_2 = |\alpha_{LO}|u(x,t)e^{-i(\omega t+\theta_0)} = |\alpha|u(x,t)e^{-i\theta}$ and the signal annihilation operator as $\hat{A}$ (from Eq. (2.70)) into the expression for homodyne photocurrent obtained in Eq. (2.65). A detailed treatment can be found in the Ref [36]. Another assumption inherent in the expressions for measured quadrature (Eq. (2.71) and (2.72)) is that the homodyne detector time resolution is sufficient such that the output photocurrent can be integrated over the temporal mode of the signal.

It turns out that determining the single photon TMF $\phi(t)$ is an important and challenging task. In Chapter 3, we shall explain our experimental technique which can be used to determine the TMF of a single photon in any unknown temporal mode, pure or non-pure.

Chapter 3

Polychromatic optical heterodyne tomography (POHT)

As discussed in chapter 1 and in section 2.3.2, having information about the temporal mode of a single photon is crucial in implementing measurements on the single photon such as quadrature measurement using homodyne detector or in general for implementing single photon or single photon qubit based quantum optical techniques such as quantum communication, quantum teleportation, quantum memory, quantum repeaters and quantum computing protocols. Eq. (2.70) is key to dependence of any measurement on the temporal mode of the single photon. Section 2.3.1 dealt with finding out the quadratures for state reconstruction if the temporal mode is known. However, in this chapter and the next, we shall look in-depth at the theory and implementation details of our technique, which we call *Polychromatic optical heterodyne tomography*, that can be used in an opposite circumstance i.e., to determine an unknown temporal mode structure from quadrature data.

3.1 Theoretical details

3.1.1 Notation details

The pure temporal mode of a photon is defined by the annihilation operator as defined in Eq. (1.1) where $\phi(t)$ is the TMF and $\hat{a}_t$ is the instantaneous annihilation operator [1] at time

[1] the concept of single photon at an instant is ill-defined. It is only approximately valid as long as the spectral width of the photon is less than its frequency. Refer Fedorov *et. al.* [37] for detailed discussion on this matter.

t. A single photon in this mode may then be written as

$$\begin{aligned} |1\rangle_\phi &= \hat{A}^\dagger |0\rangle \\ &= \int_{-\infty}^{\infty} \phi^*(t)\hat{a}_t^\dagger |0\rangle \, dt \end{aligned} \tag{3.1}$$

In actual laboratory setups, the electronics used in the measuring systems have a finite resolution due to their bandwidth and also due to their memory buffer structure. In simple words, it implies that for measuring photocurrent corresponding to the signal photon over a certain time interval, there are finite number of data points that can be taken. This gives us the concept of time-bins as a consequence of the discussed detector electronics resolution. Due to this digital nature of our data acquisition system, we can convert the integration in Eq. (3.1) to a summation over the time bins as

$$|1\rangle_\phi = \sum_k \phi^*(t_k) \, |1_k\rangle \tag{3.2}$$

such that normalization holds for $\phi(t)$ as

$$\sum_k |\phi(t_k)|^2 = 1 \tag{3.3}$$

In the notation used in Eq. (3.2), t_k represents the k^{th} time-bin and $|1_k\rangle$ is the state containing one photon in the k^{th} time bin and vacuum in all other bins. As a general convention for the rest of the text, it shall be assumed unless mentioned otherwise that $|n_k\rangle$ is a state containing n photons in the k^{th} time-bin. The creation operator in general for the k^{th} time bin would obey the following relationship

$$\hat{a}_k^\dagger |n_j\rangle = (1 - \delta_{jk}) \, |1_k n_j\rangle + \delta_{jk}\sqrt{n+1} \, |(n+1)_j\rangle \tag{3.4}$$

In general, for any single photon state, with pure or non-pure modal structure, the density operator completely characterizes the state. It can be represented as $\sum_{mn} \rho_{mn} \, |1_m\rangle \langle 1_n|$, where ρ_{mn} is the TDM in the time-bin basis. For photons with non pure modes, the TDM

can also be expressed a statistical mixture of pure modes. In the diagonal representation, it looks like

$$\hat{\rho}_{t_i,t_j} = \sum_k p_k \phi_k^*(t_i)\phi_k(t_j), \tag{3.5}$$

where, p_k is the eigenvalue or weight of the k^{th} mode $\phi_k(t)$. Having defined the convention in the present section, the next one focuses on the theory behind the technique of POHT.

3.1.2 Theory

The technique of POHT uses multiple LO frequencies for homodyne measurements and extracts the TDM of the prepared single photon from the autocorrelation statistics of the homodyne photocurrent. The output photocurrent from the homodyne detector for the j^{th} time-bin $I(t_j)$ is proportional to the quadrature

$$\hat{X}_j = (\hat{a}_j e^{-i(\theta_j)} + \hat{a}_j^\dagger e^{i(\theta_j)})/\sqrt{2} \tag{3.6}$$

where $\theta_j = \delta\omega \cdot t_j + \theta_0$ is the optical phase difference between the LO and the signal. Here $\delta\omega$ is the frequency detuning between the LO and the signal and θ_0 the LO relative phase at $t = 0$. . The autocorrelation matrix for the homodyne current is then

$$\langle I(t_j)I(t_k)\rangle \propto \langle \hat{X}_j\hat{X}_k\rangle = \mathrm{Tr}[\hat{\rho}\hat{X}_j\hat{X}_k] = \sum_{mn} \rho_{mn} \langle 1_n| \hat{X}_j\hat{X}_k |1_m\rangle , \tag{3.7}$$

where each matrix element can be evaluated using Eq. (3.4) and Eq. (3.6) as

$$\begin{aligned}
\langle 1_n|\,\hat{X}_j\hat{X}_k\,|1_m\rangle &= \langle 1_n|\,\hat{X}_j\frac{(\hat{a}_k e^{-i(\theta_k)}+\hat{a}_k^\dagger e^{i(\theta_k)})}{\sqrt{2}}\,|1_m\rangle \\
&= \frac{1}{\sqrt{2}}\,\langle 1_n|\,\hat{X}_j\left(\delta_{km}(|0_k\rangle\,e^{-i\theta_k}+\sqrt{2}\,|2_k\rangle\,e^{i\theta_k})+(1-\delta_{km})\,|1_k1_m\rangle\,e^{i\theta_k}\right) \\
&= \frac{1}{2}\,\langle 1_n|\,(\hat{a}_j e^{-i(\theta_j)}+\hat{a}_j^\dagger e^{i(\theta_j)})\cdot \\
&\quad \left(\delta_{km}(|0_k\rangle\,e^{-i\theta_k}+\sqrt{2}\,|2_k\rangle\,e^{i\theta_k})+(1-\delta_{km})\,|1_k1_m\rangle\,e^{i\theta_k}\right) \\
&= \frac{1}{2}\,\langle 1_n|\,\Bigg[2\delta_{km}\delta_{jk}e^{i(\theta_k-\theta_j)}\,|1_k\rangle+(1-\delta_{km})\delta_{jk}e^{i(\theta_k-\theta_j)}\,|1_m\rangle \\
&\quad +(1-\delta_{km})\delta_{jm}e^{i(\theta_k-\theta_j)}\,|1_k\rangle+\delta_{km}e^{i(\theta_j-\theta_k)}\,|1_j\rangle+\sqrt{2}\sqrt{3}\delta_{jk}e^{i(\theta_k+\theta_j)}\,|3_k\rangle \\
&\quad +(1-\delta_{jk})\sqrt{2}e^{i(\theta_k+\theta_j)}\,|1_j2_k\rangle+(1-\delta_{km})\delta_{jk}e^{i(\theta_k+\theta_j)}\,|2_k1_m\rangle \\
&\quad +(1-\delta_{km})\delta_{jm}e^{i(\theta_k+\theta_j)}\,|1_k2_m\rangle+(1-\delta_k m)(1-\delta_{jk})(1-\delta_{mk})\,|1_j1_k1_m\rangle\Bigg] \\
&= \frac{1}{2}\Bigg[2\delta_{km}\delta_{jk}e^{i(\theta_k-\theta_j)}\delta_{kn}+(1-\delta_{km})\delta_{jk}e^{i(\theta_k-\theta_j)}\delta_{mn}+(1-\delta_{km})\delta_{jm}e^{i(\theta_k-\theta_j)}\delta_{kn} \\
&\quad +\delta_{km}e^{i(\theta_j-\theta_k)}\delta_{jn}+0\Bigg] \qquad (3.8)
\end{aligned}$$

The 0 obtained in the last step comes from the terms for which the inner product goes to zero. Substituting the relative optical phases $\theta_t = \delta\omega\cdot t$ as discussed in section 2.3.1 (see Eq. (2.67)), and canceling out the redundant *Kronecker-delta* functions we obtain

$$\langle 1_n|\,\hat{X}_j\hat{X}_k\,|1_m\rangle = \frac{1}{2}\left[e^{-i\delta\omega(t_k-t_j)}\delta_{km}\delta_{nj}+\delta_{jk}\delta_{nm}+e^{-i\delta\omega(t_j-t_k)}\delta_{jm}\delta_{nk}\right] \qquad (3.9)$$

Note that Eq. (3.9) does not depend on any initial phase θ_0 of the coherent state due to the phase uncertainty of Fock states. We can perform the summation over m, n in Eq. (3.7) using Eq. (3.9) as

$$\begin{aligned}
\sum_{mn}\rho_{mn}\,\langle 1_n|\,\hat{X}_j\hat{X}_k\,|1_m\rangle &= \frac{1}{2}\sum_n\left[\rho_{kn}e^{-i\delta\omega(t_k-t_j)}\delta_{nj}+\rho_{nn}\delta_{jk}+\rho_{jn}e^{-i\delta\omega(t_j-t_k)}\delta_{nk}\right] \\
&= \frac{1}{2}\left[\rho_{kj}e^{-i\delta\omega(t_k-t_j)}+\delta_{jk}\sum_n\rho_{nn}+\rho_{jk}e^{-i\delta\omega(t_j-t_k)}\right] \qquad (3.10)
\end{aligned}$$

Using the information that the TDM is normalized and Hermitian,

$$\sum_n \rho_{nn} = 1 \tag{3.11}$$

$$\rho_{jk} = \rho^*_{kj} \tag{3.12}$$

we obtain from Eq. (3.10),

$$\langle \hat{X}_j \hat{X}_k \rangle = \frac{1}{2}\delta_{jk} + A_{jk}. \tag{3.13}$$

The first term in Eq. (3.13) corresponds to the autocorrelation matrix for the vacuum. The second term, which we call the *reduced* autocorrelation matrix, is directly related to the photon's TDM:

$$A_{jk} = \mathrm{Re}[\rho_{jk}] \cos[\delta\omega(t_j - t_k)] + \mathrm{Im}[\rho_{jk}] \sin[\delta\omega(t_j - t_k)]. \tag{3.14}$$

If the LO frequency is same as that of the signal, i.e., at $\delta\omega = 0$, the autocorrelation matrix depends only on the real part of the TDM. However, by using $\delta\omega \neq 0$ one obtains access to its imaginary part. Eq (3.14) is the crux of our method of POHT because when the detuning $\delta\omega$ is non-zero, then the dependence of the autocorrelation matrix on both real and imaginary parts of the TDM allows us to access the complete complex TDM of the single photon.

3.2 Experiment

3.2.1 Experimental setup

The experimental setup is shown in 3.1. We start by generating the two-mode squeezed vacuum state from the FWM setup in atomic vapor as discussed in section 2.2.2.2. We use coherent double Raman scattering (four-wave mixing) in an ensemble of Λ-type atoms (see Fig. 2.1b for the energy level diagram) to generate a two-mode squeezed state in a non-degenerate phase-matched configuration [38]. A hot ^{85}Rb vapor cell is pumped by a 1.2 Watt laser beam at 795 nm derived from a continuous-wave Tekhnoscan TIS-SF 777

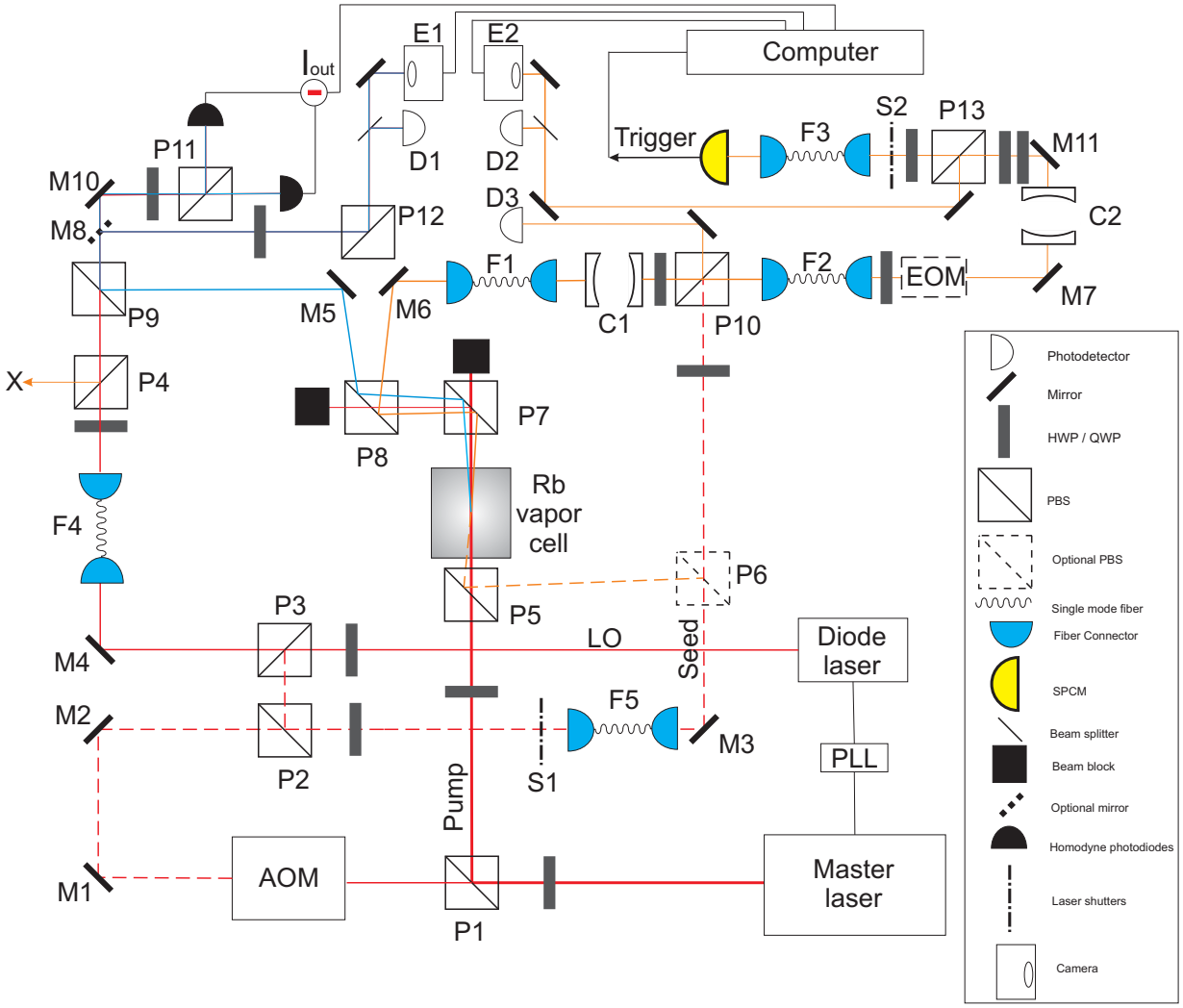

Figure 3.1: Outline of our experimental setup - (EOM: electro-optic modulator; SPCM: single photon counting module; C1, C2: filter cavities; PLL: phase lock loop; AOM: acousto-optic modulator; E: Camera; D: photodiodes; P: PBS; F: single mode optical fiber;M: mirrors). The master laser generates the pump beam and the phase-locked diode laser generates the LO beam. The signal (blue) goes to the homodyne detector, whereas the idler beam (orange) passes through C1 (55 MHz) and C2 (7 MHz) before detection on a SPCM. The EOM between C1 and C2 is optional. All optional components and optical paths are shown with dashed line.

Ti:Sapphire master laser. The signal and idler beams are spatially separated from the pump, and a specific spatial mode is selected in the idler channel using a single-mode fiber (F1). Subsequently, the idler channel is subjected to spectral filtering by means of a lens cavity (C1) of a 55 MHz bandwidth [39] and a conventional Fabry-Perot cavity (C2) of bandwidth $\gamma/2\pi = 7$ MHz. The usage of two cavities with incommensurate free spectral ranges ensures that the combined spectral filter has a single transmission peak of 7 MHz width. The task of cavity C1 is to eliminate any residual pump photons which may have propagated into the idler channel because of imperfections or instability in polarization of the pump photons causing some of them to escape transmission through the PBS P7 and P8. At the same time the cavity C1's linewidth is comparable to FWM bandwidth (about 50 MHz). This is another reason why the effect of cavity C1 on the temporal mode structure of the remotely prepared photons is negligible.

The idler beam is then coupled to a PerkinElmer single photon counting module (SPCM) with a dark count rate below 100 Hz. Both cavities are maintained at a stable frequency by using an alignment beam (seed) which is unblocked every few seconds to monitor and readjust the laser to the cavity resonance frequency. Detection of an idler photon projects the signal onto a single photon in a well-defined spatio-temporal mode conjugate to the idler. The spatial mode is selected by the placement of the guiding single mode fibers in the idler channel. This signal channel is mode-matched with a continuous-wave LO (18 mW) for homodyne detection [18]. The LO is derived from a diode laser that is locked and phase stabilized with respect to the pump using an optical phase-lock loop (PLL) [40].

A seed beam is used in the idler channel for alignment purposes as the flux of single photons generated by FWM is so small that it is impossible to observe the beam with naked eye or classical detectors. The seed beam is a weak coherent beam but strong enough so as to allow us any classical alignment of the experimental setup. It can be derived from either the master laser through an acousto-optic modulator (AOM) or through the LO beam. We

ensure that the seed beam and the idler beam are almost mode matched spatially by the following procedure. The set of mirrors represented by M3 is used in conjunction with the PBS P6 and P5 to align the seed beam. A camera (not shown in the figure) is placed after P8 in the reflected channel. The transverse profile of the signal, idler and the residual pump beam can be seen on the camera. The seed is adjusted so as to maximize the signal beam intensity. Among other things to take care of is the relative symmetric alignment of the seed, signal and residual pump. A symmetrically positioned Gaussian transverse profile of the signal beam with a gain of almost one signifies good alignment of the vapor cell for phase-matching. Apart from that the seed is used for classical aligning the cavities C1 and C2 so as to transmit the Gaussian beam through the fundamental TE mode of the cavity. Another use of the seed beam is to maximize the coupling of single mode fiber F1, F2 and F3. One may also block the output of the AOM and then scan the LO beam across the idler frequency using the laser controller so as to determine the transmission spectrum of cavity C1. A laser shutter [41] in the seed channel is used for blocking the seed beam while data acquisition is active so as to protect the SPCM.

3.2.2 Performing the experiment

3.2.2.1 Aligning the homodyne detector

Assuming that the pump laser is lasing at the desired frequency and with about 1.2 Watt of power, the first step in performing the experiment is to align the setup without cavity C2 and EOM to obtain maximum single photon efficiency. To this end, LO and the signal beams are spatially mode matched with the help of camera E1 and photodetector D1. The signal beam is very weak. So we use stimulated FWM, where the seed beam (dashed orange line) is sent along the idler channel through the ^{85}Rb vapor cell. Once that is ensured, the homodyne detector is balanced with the help of LO beam with the signal beam blocked. To ensure that the detector is balanced, we look at the output of the homodyne on an oscilloscope which should be as less as possible (10 mVp-p in our case). We then check the output spectrum

of the homodyne detector on a spectrum analyzer which should be almost a plateau in the region of 1-100 MHz [18]. If the output has some peaks in the plateau region, possible reason could be unequal optical path length in the two arms leading to a mismatch in their arrival times causing beats. Aligning the homodyne can get rid of such noise. We observed that the characteristic shape of the plateau changed if the LO strength was not sufficient. In our case we used $\sim$ 18 mW of LO power.

3.2.2.2 Monitoring single photon efficiency without narrowband cavity

The purpose of this step is to verify that the single photon detection efficiency is good enough for the experiment to be carried out. Only cavity C2 is used in this step. The bandwidth of the cavity is comparable to the bandwidth of the FWM process while its main function is to filter out the residual pump photons. Because of comparable bandwidth of the cavity to that of the FWM gain bandwidth, it leaves the temporal profile of the photons generated via FWM unchanged. The expected temporal mode is assumed to be roughly Gaussian with a spread $\tau \sim 1/\Delta\nu_{\mathrm{FWM}}$. The knowledge of the approximate temporal mode allows us to calculate quadratures in real time (using Eq. (2.71)) for estimating the single photon efficiency in real time. The procedure and the underlying techniques are explained further in this section.

After having aligned the homodyne and mode-matched the LO and the signal beam we open the signal channel and connect the output of cavity C1 directly to the SPCM using the single mode fiber F2. Before switching on the SPCM we ensure that the seed beam is blocked at multiple points including the part of LO that contributes towards the seed beam and that the AOM beam is off. The SPCM trigger and the homodyne output are capable of being delayed in time with respect to each other with the help of self designed data acquisition software and externally through BNC cables. Once the SPCM is on, we can roughly monitor the single photon efficiency by using our self made software[42]. The software works on the following principle. Upon receiving the a trigger from the SPCM, it

is able to acquire certain number of homodyne data traces of certain duration (usually a few hundred nanoseconds) each centered around the trigger point which is defined as the point when the 'click' from the SPCM is detected. From the acquired traces it calculates the quadrature[2] from Eq. (2.71) from which it can find out the variance in quadrature of the acquired traces. At the start of the alignment process, the signal is blocked such that the data acquired corresponds to the vacuum state. The variance of vacuum calculated from there serves a benchmark for calculating the single photon efficiency. With the signal unblocked, the software keeps acquiring batches of data corresponding to the signal and compares the variance in the quadratures of signal with that of the vacuum data acquired earlier. It then updates in real time the single photon efficiency on the computer display. It must be emphasized here that the efficiency displayed by the software is an approximate measure because we use a guess temporal mode which can be approximately calculated from the bandwidth of the FWM process and the lens cavity linewidth.

The purpose of monitoring the efficiency is to carry out the alignment of the signal beam and the idler beam for maximizing the single photon detection efficiency. To align the signal beam one uses mirrors and lenses after the intercepting mirror (M5) and before the PBS (P9). For aligning the idler beam one can use the mirrors and lenses between intercepting mirror (M6) and fiber connector before single mode fiber F1. The fiber determines the spatial mode of the idler and hence of the conjugate signal photons. Another fiber F2 couples the filtered single mode idler beam to the SPCM. It is assumed here that the fibers F1 and F2 are aligned with maximum coupling efficiency and that the cavity C1 transmits all the light through its fundamental Gaussian TE mode. The alignment talked about in the last sentence is completely classical and can be done with the help of the seed beam as discussed in the previous sections.

The pump laser may drift sometimes because of which the transmission through cavity C2

[2]For live data monitoring we assume a roughly Gaussian TMF with standard deviation comparable to that of the bandwidth of the FWM process as discussed in the start of this section

drops resulting in a low count rate and in loss of efficiency. For this reason, it is advisable to monitor the single photon count rate and adjust the pump frequency after every few minutes. Once maximum single photon efficiency is achieved we move onto incorporating the new cavity C2 as discussed in the next section 3.2.2.1. I would also like to mention here that the frequency of the pump corresponding to maximum count rate achievable does not necessarily correspond to maximum single photon efficiency. The reason for that is there could be Raman scattered photons which may have originated from an atom in one of the other ground states of the lambda level scheme of our system of rubidium atoms (refer to Fig. 2.1b). Such a photon is not generated by FWM process and hence there does not exist any signal photons corresponding to it. For this reason we maximize the transmission of C2 for maximum single photon efficiency and not for maximum count rate. The maximum count rate and the count rate corresponding to maximum single photon efficiency were ~ 1 MHz and ~ 250 KHz respectively in the actual experiment. It is for this reason that the seed beam which is used aligning any cavity in the idler channel is red detuned from the pump by about 3.036 GHz (conjugate to the blue detuning of signal and LO from pump) whereas the gain profile maximum for the idler beam is red detuned from the pump by 3.072 GHz. The blue detuning of the seed by 40 MHz from the maximum of the gain profile of the idler is to eliminate the effect of the stray Raman scattered photons.

3.2.2.3 Aligning the narrowband cavity C2

The goal of the cavity C2 is to stretch the remotely prepared signal photon in time domain thereby allowing it to be resolved by the homodyne detector electronics (See section 4.3.1 for theoretical details). First step in incorporating the new cavity is to align it for maximum transmission of the idler beam through its TE_{00} mode. Since the actual idler beam is very weak, so we use the *seed* beam. The actual idler frequency mode chosen is conjugate to the frequency mode of the LO which is centered at the signal frequency. In our case the LO is blue detuned to the pump by $|\omega_s - \omega_p|$ which is the same as the seed is red-detuned from

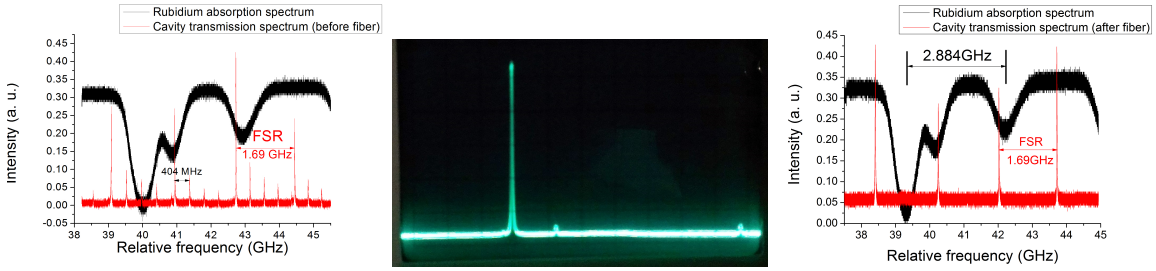

(a) Before F3 (b) Before F3, well aligned (c) After F3

Figure 3.2: Cavity C2 transmission spectrum. (a) Forward transmission spectrum (red) for a fairly misaligned cavity compared against ^{85}Rb absorption spectrum (black). The frequency scale is not absolute. (b) Actual C2 forward transmission spectrum for a fairly well-aligned cavity. (c) Transmission spectrum of cavity C2 after passing it through the single mode fiber F3 resulting in the suppression of any other spatial mode than TE_{00} shown by narrow (red) peaks. Black line shows the^{85}Rb absorption spectrum to serve as a scale.

the pump.

To align the cavity one uses the mirrors and lenses after the coupling fiber F2 and before the cavity. One of the cavity mirrors is mounted on a piezoelectric mount and can be oscillated to scan the cavity frequency across several FSR. The signal from the cavity is sent to a photodetector (D2) and a camera (E2). The output of the photodetector can be monitored on an oscilloscope. The transmission spectra of the cavity (obtained from the photodetector D2) before and after the SMF F3 is shown in Fig. 3.2(a)(c). Fig 3.2(b) shows the transmission spectra of a well aligned cavity where only the fundamental TE_{00} mode is being transmitted through and all other spatial transmission modes suppressed. The camera E2 output further helps in verifying that the transverse profile of the transmitted beam corresponds to a TE_{00} mode. For aligning the cavity's fundamental TE mode with the single mode fiber F3, a few microwatts output X of the local oscillator from P4 is sent backwards into the cavity through F3 while the input from F2 is manually blocked. A QWP is needed between C2 and P13 so as to see the back-reflected beam on the camera (E2) and detector (D2). The back-reflected and the forward reflected spectrum should look alike as in Fig 3.2b if the alignment beam used are of the same frequency. However, in our case the LO beam (X) used for backward alignment and the seed beam for forward alignment are of different

frequencies, therefore the spectra although being alike was shifted with respect to each other by the seed-LO detuning.

Once the cavity is aligned, we carefully disconnect the end of fiber F3 from fiber coupler X and connect it back to the SPCM. Care is taken not to disturb the end of F3 connected to cavity-side (C2).

3.2.2.4 Preliminary tests before data acquisition

Before acquiring any data the shutters [41] are tested for any faults in their response time or vibration insulation mechanism. If needed the shutters may have to be realigned for a faster response time or their vibration insulation pads changed.

The next step is to verify if the setup is still aligned well for a good single photon efficiency. For that we manually repeat the procedure as discussed in section 3.2.2.2 except for the difference of SPCM detection after fiber F3 instead of F2. We noticed an efficiency of about 9 percent[3] (as displayed by our program) and a reduced count rate of 4(1) KHz without(with) the optional EOM[4]. In case of lower efficiencies there may have been possibilities of laser drifting or the setup being misaligned somehow. A failure in debugging this situation may involve repeating steps from section 3.2.2.2 onwards.

Once all the said steps have been carried out successfully, the final test would be to run a few dummy instances of the modified data acquisition software integrating shutter operation with the data acquisition. The sequence is explained in the next section. If everything works well in the few dummy runs, data acquisition can be started.

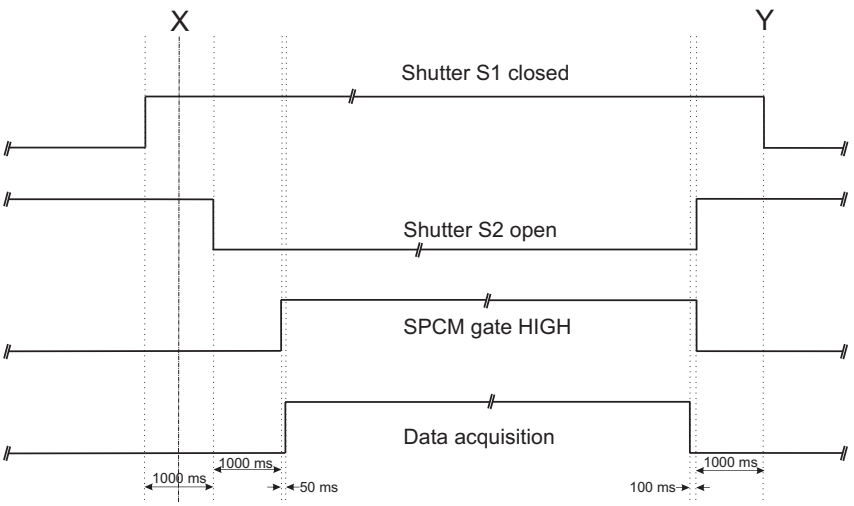

Figure 3.3: Experimental sequence: (*top to bottom*) laser shutter S1 to block seed, laser shutter S2 to block SPCM input, SPCM gate signal and data acquisition. For shutters HIGH(LOW) = block(unblock); SPCM gate: HIGH = active; data acquisition: HIGH = active.

3.2.2.5 Data acquisition process

The data acquisition sequence is showed in Fig 3.3. The sequence starts at the vertical line 'X' with both shutters closed, SPCM gated LOW (corresponding to SPCM off). A delay of 1000 ms after a shutter's opening or closing avoids the effects of vibration if any, caused by operation of the laser shutters fixed upon the optical table. The delay of 50 millisecond after SPCM is gated high is to avoid slow gating response time. The delay of 100 ms is to allow the computer to save any data which is still in the memory buffer of the acquisition card. At the end of the sequence represented by 'Y' in the figure, the software halts the acquisition for user's input.

The user would be able to monitor the transmission of the seed beam through the cavity C2 by using camera E2 once the shutter S1 is unblocked after S2 gets blocked. The output

[3]This efficiency is not the actual efficiency because our software is programmed to calculate the quadratures over the approximate temporal mode discussed in section 3.2.2.1

[4]The alignment of optical fiber attached to EOM on both ends is assumed to be trivial and is explained here in short. The fiber F2 is removed to accommodate EOM. The HWP before the EOM is changed in conjunction with the amplitude of the modulating voltage applied to it to get the desired modulation. The waveform after modulation can be checked by looking at the forward transmission spectrum of the cavity C2. The scanning rate should be low in general (∼20 Hz), otherwise, the response time of the piezoelectric transducer may broaden the peaks of the spectrum.

of the camera E2 gives the transverse intensity profile of the transmitted seed beam through the cavity C2. The maximum of transverse intensity profile can be kept track of so as to monitor the cavity transmission.

The SPCM count rate during data acquisition HIGH also gives some information about the cavity transmission level. In case the cavity C2 transmission drops, first the transmission of cavity C1 is maximized by changing the pump frequency and monitoring the transmission through the photodetector D3. The reason behind this is that the master laser may have got unlocked or drifted in frequency due to any temperature changes or vibration caused by the shutter operation. After cavity C1 has been adjusted the HWP after C2 in turned so that the idler beam goes through to the detector D2 and camera E2. In our case, the HWP before the PBS P13 is set to transmit more than 95 percent through towards SPCM via shutter S2 an SMF F3. The remaining is always available for monitoring the C2 transmission between batches of data acquisition. This eliminates the need for manual adjustment of the HWP for monitoring cavity transmission. This ensures that the single photon efficiency is not lost while data acquisition can be done at a good pace. The DC voltage applied on one of the cavity C2 mirrors driven by a piezoelectric element allows one change the length of the cavity thereby changing the resonance frequency so as to maximize the cavity C2's transmission through the fundamental mode of the cavity. Once the user is sure that everything is working well, he initiates the next sequence of data acquisition and this process goes on. Each such sequence acquires about 10^4 traces of homodyne photocurrent. The time taken for acquiring a batch of 10^4 traces is small enough for the cavity transmission to remain stable during that duration.

For each individual trace, a click from the SPCM in the idler channel acts as the trigger for the measurement of the signal. The homodyne photocurrent is recorded for 360 ns around the trigger point as reference with a time binning of 2 ns. The time interval for which the data is recorded may vary depending upon the buffer memory characteristics of the acquisition

card. In our case, single photon's temporal profile estimated from the inverse bandwidth of cavity C2 was of the order of 10^2 ns. Our card allowed us to record a maximum of 180 data points per trace thereby making 2 ns resolution a good choice to capture the complete temporal profile.

For each LO detuning, the autocorrelation matrix given by Eq. (3.13) of the homodyne photocurrent is obtained by taking an average of the autocorrelation matrix over 2 million traces acquired from executing 200 data acquisition sequences. After the data acquisition for each LO frequency, the signal is blocked and two long sequences of data acquisition take a million traces of vacuum photocurrent. The purpose of this is to estimate and eliminate the vacuum background. It turns out that there is a much simpler procedure for eliminating any vacuum contribution and any offset homodyne photocurrent which will be discussed in the next chapter, section 4.1. To compare the vacuum noise with the noise due to any thermal background[5], we acquire 2 million data sets with randomly spaced trigger events (with the help of a function generator) with about the same mean frequency as the average count rate registered while acquiring the signal data. The signal beam is unblocked for thermal data.

3.2.2.6 Electrooptic modulator

Another component of our experimental system is an electrooptic modulator (EOM). The task of this device is to induce phase modulation along a particular polarization axis. It works as follows. At its heart it contains a birefringent crystal. A modulating voltage is applied to the EOM. The field is applied by means of a capacitive plate like structure between which the crystal is sandwiched. Depending upon the strength of the applied field the refractive index along one of the axes changes. This axis usually matches the polarization maintaining

[5]Thermal noise is a statistical mixture of fock states following the following representation:

$$\hat{\rho} = \frac{1}{\zeta} \sum_{n=0}^{\infty} \left(\frac{\zeta - 1}{\zeta} \right)^n |n\rangle \langle n| ,$$

where $\zeta = \frac{1}{1 - e^{-\frac{\hbar\omega}{k_B T}}}$, T called the thermal state temperature. For more details about thermal light see Ref. [43]. Such a mixed state is generated by randomly emitting incoherent sources of photons such as a light bulb.

axis of the optical fiber input. The phase of the modulating voltage is key to the strength of electric field and it plays an important role in making temporal mode structure of a phase modulated photon from a non-deterministic source such as FWM non-pure. As we would discuss later in section 4.3.2, the phase modulation setup such as ours in conjunction with random arrival time of the single photon makes the modal structure of the remotely prepared photon mixed.

Chapter 4

Calculations, Results and Discussions

4.1 Autocorrelation matrix

The homodyne photocurrent traces acquired in the experiment are 360 ns long with a time binning of 2 ns. The motivation for the chosen time scales was discussed in section 3.2.2.5. The autocorrelation matrix is calculated for each trace. The average over 2 million traces recorded per LO detuning gives us the final autocorrelation matrix corresponding to Eq. (3.13) for that detuning. We then process them to eliminate the vacuum term in Eq. (3.13), as well as any contributions from the DC bias in the homodyne photocurrent and thermal background. These contributions are not correlated with trigger events, and should be constant along $t_j - t_k$ excluding the negligible high frequency noises. This can be confirmed by the autocorrelation of randomly triggered data which corresponds to measurements on signal channel with arbitrary trigger pulses generated by a function generator. The point-wise variance of the homodyne photocurrent for a heralded signal photon, vacuum and for the randomly triggered data is shown in Fig. 4.1.

We calculate the mean value of the autocorrelation matrix along the line $t_j - t_k$ = constant and t_i, t_j lying significantly[1] after the trigger instant where there are no signal photons. This ensures that the mean value corresponds to just the vacuum contribution and any possible offset in the homodyne photocurrent. Calculating it along the lines parallel to the diagonal ensures that any high frequency noise which lies outside the bandwidth of the homodyne detector is also eliminated. Subtracting the mean from the respective lines of the autocorrelation matrix yields the reduced autocorrelation matrix. Fig. A.1 and A.2 show

[1] see equation (4.5), t > 0 corresponds to no photons. Because of the finite response time of the homodyne detector, the Heaviside function loses its steep rise. So to be explicit about not including any single photon component in the mean subtraction, we consider t$\gg$0. Also, see description of Fig 4.1

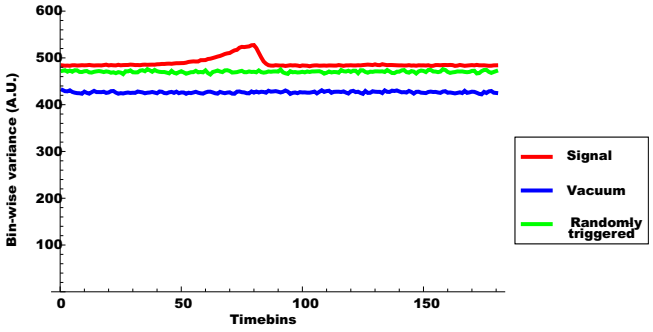

Figure 4.1: Point-wise variance of the homodyne photocurrent for heralded single photons in the signal channel (red), vacuum state (blue) and for randomly triggered data (green) calculated over 2 million homodyne photocurrent traces. The offset due seen is due to the vacuum state contribution, any offset current output from the homodyne and thermal noise contribution. It can be eliminated by mean subtraction. It must be noted that for time-bins much after the trigger (77^{th}) the offset is common for single photon and randomly triggered data. This fact is used for elimination of the constant term and other offset bias from Eq. (3.13). In the above figure, time-bins > 100 shows the region of interest for calculation of offset from the signal trace.

the autocorrelation and reduced autocorrelation matrices for the case of unmodulated and phase modulated single photon.

Comparision with the theory: To check the compatibility of our results with the theoretical expressions, we derive the reduced autocorrelation matrix theoretically and compare it with the experimentally obtained data. To do so, we calculate the TMF from the knowledge of the experimental setup (see section 4.3). Utilizing diagonal representation of TDM (see Eq. (3.5)) we calculate the theoretical value using the obtained theoretical TMF. From the theoretical TDM we calculate the reduced autocorrelation matrices according to Eq. (3.14). To make the theoretically obtained result closer to the observed reduced autocorrelation we take into account the finite gain bandwidth of the FWM process (see Fig. 2.1c) by means of an appropriate convolution of the temporal mode with the FWM gain profile. The comparison of theoretical and experimental reduced autocorrelation matrices for the setting of unmodulated photon is shown in Fig. 4.2.

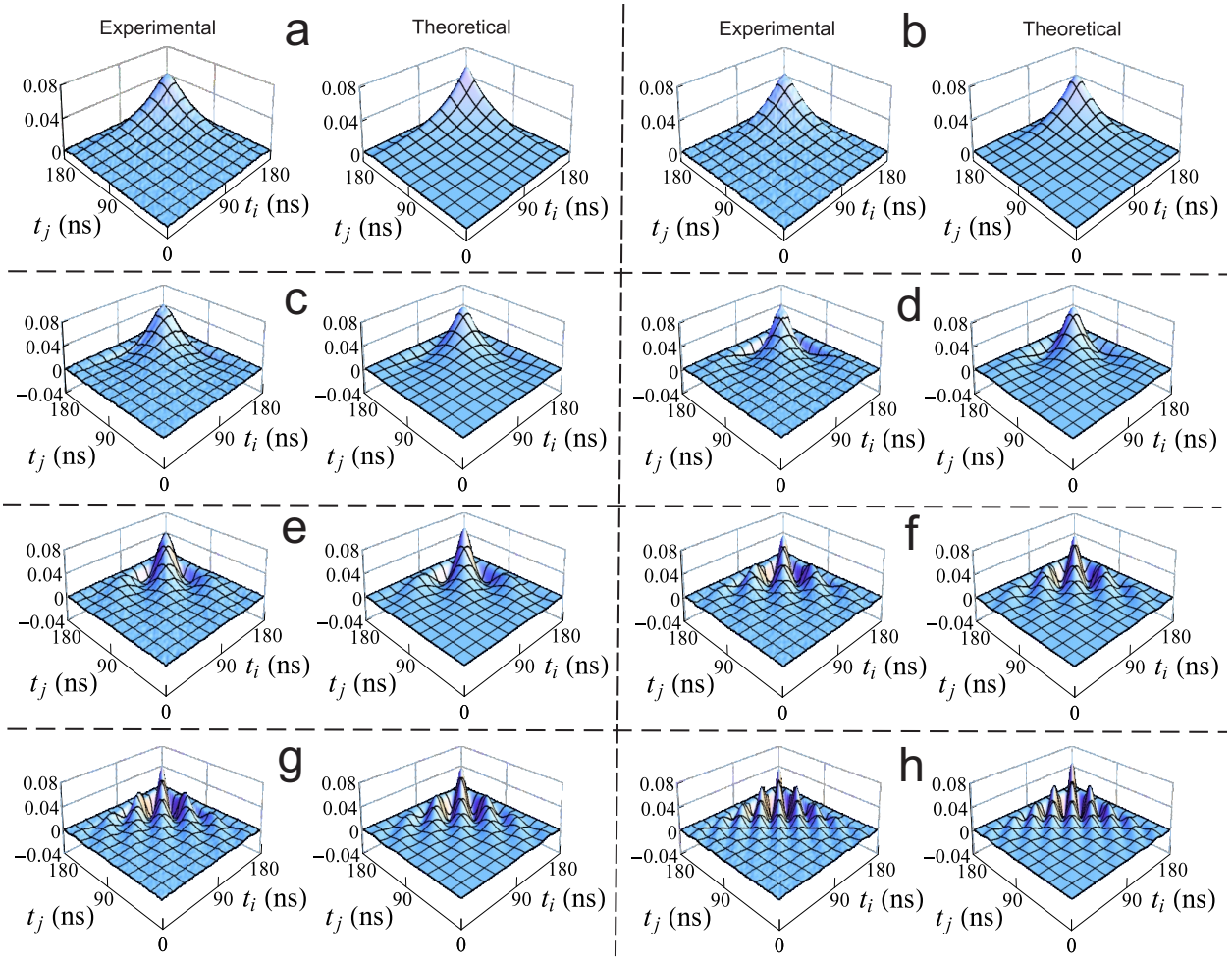

Figure 4.2: Theoretical (right) and experimental (left) reduced autocorrelation matrices for the case of unmodulated photon, for different LO detuning: (a) 0 MHz, (b) 1.8 MHz, (c) -5.1 MHz, (d) 7.2 MHz, (e) -10.8 MHz, (f) 16.2 MHz, (g) 19.2 MHz and (h) 27 MHz, corresponding to the measurement setting without modulation. The trigger photon arrives at $t = 155\ ns$.

4.2 Extraction of experimental TDM

Once the reduced autocorrelation matrices have been calculated, the TDM can be determined by solving Eq. (3.14) for each pair (j, k). However, such direct approach does not ensure positivity and normalization of the reconstructed density operator. To incorporate these *a priori* constraints into the reconstruction, we implement a more sophisticated iterative optimization algorithm based on machine learning. The algorithm uses the eight experimental reduced autocorrelation matrices as the training set. We take only the relevant area of the autocorrelation matrix to reduce the time and memory complexity of the algorithm. We start from an initial Hermitian guess estimate of the TDM which for example could be an identity matrix. The difference between the experimental left-hand side of Eq. (3.14) and the right-hand side of that equation evaluated from the estimated TDM, squared and summed over all pairs (j, k) and all LO frequencies, is used as the cost function. Iterations utilize the diagonal representation of the TDM: $\hat{\rho} = \sum_i p_i \left|\psi_i\right\rangle \left\langle\psi_i\right|$. In the first step of each iteration, the eigenvalues p_i are adjusted to minimize the cost function while keeping them real, non-negative and totaling 1. In the second step, the eigenvectors $\left|\psi_i\right\rangle$ are optimized by pairwise unitary transformations. The process is repeated until the cost function asymptotically converges to give the best fit of the TDM.

4.3 Theoretical TMF and TDM

4.3.1 For unmodulated photon

The theoretical TMF for an unmodulated single photon can be obtained as follows. The bi-photon generated by the four-wave mixing process with an infinite gain bandwidth can be represented as

$$\left|\Psi\right\rangle = \int \left|1_{\omega_s}, 1_{\omega_i}\right\rangle \delta(\omega_s + \omega_i - 2\omega_p) d\omega_s d\omega_i \tag{4.1}$$

where indices s, i and p correspond to signal, idler and pump respectively. The amplitude transmission function of the cavity in the neighborhood of its resonance can be expressed as a function of the detuning of the beam from the cavity resonance frequency $\delta_i = \omega_c - \omega_i$ as $T(\delta_i) = \sqrt{2/\pi\gamma}(1 - 2i\delta_i/\gamma)^{-1}$, where γ is the linewidth of the cavity C2. Subjecting the idler channel to transmission through this cavity, state (4.1) transforms into:

$$|\Psi'\rangle = \sqrt{\frac{2}{\pi\gamma}} \int \frac{1}{1 - 2i\frac{\delta_i}{\gamma}} \delta(\omega_s + \omega_i - 2\omega_p) \, |1_{\omega_s}, 1_{\omega_i}\rangle \, d\omega_s d\omega_i. \tag{4.2}$$

Subsequent idler photon detection at time t_i will project the signal onto the state $|1\rangle_{\phi_s} = \langle 1_{t_i} \, | \, \Psi' \rangle$ where $|1_{t_i}\rangle = \int |1_{\omega_i}\rangle \, e^{i\delta_i t_i} d\omega_i$. Assuming that the detection event happens at $t_i = 0$, the resultant state in the signal channel in the frequency domain can be expressed as

$$|1\rangle_{\phi_s} = \langle 1_{t_i=0} \, | \, \Psi' \rangle = \sqrt{\frac{2}{\pi\gamma}} \int \frac{1}{1 + 2i\frac{\delta_s}{\gamma}} \, |1_{\omega_s}\rangle \, d\omega_s, \tag{4.3}$$

where $\delta_s = 2\omega_p - \omega_c - \omega_s$ is the detuning of the signal frequency from the central frequency determined by the cavity. Performing a Fourier transform on Eq. (4.3), we find the temporal mode of the signal photon as:

$$|1\rangle_{\phi_s} = \sqrt{\gamma} \int e^{\gamma t_s/2} \Theta(-t_s) \, |1_{t_s}\rangle \, dt_s \tag{4.4}$$

where $\Theta(\cdot)$ is the step function. This rising exponential mode is similar to that of a cavity enhanced photon studied in Ref. [44]. Using the definition of temporal mode from Eq. (3.1), we obtain

$$\phi(t) = \sqrt{\gamma} e^{\gamma t/2} \Theta(-t), \tag{4.5}$$

The primary element determining the mode of the heralded photon is the narrowband filter cavity C2 in the idler channel. Additionally, the mode's bandwidth is limited by the ~ 50 MHz gain bandwidth of the FWM process used to generate the bi-photons. This effect is taken into account by an appropriate 2D Gaussian time convolution in all the theoretical autocorrelation plots presented, however we neglect it in any theoretical expressions for clarity. The TDM is obtained from Eq. (3.5) by considering the discretized version of mode

$\phi(t)$ from Eq. (4.5). Taking into account the bandwidth of the FWM process brings the theoretical TDM closer to the observed TDM. Fig. 4.3 shows the comparison of experimental and theoretical results for the unmodulated photon.

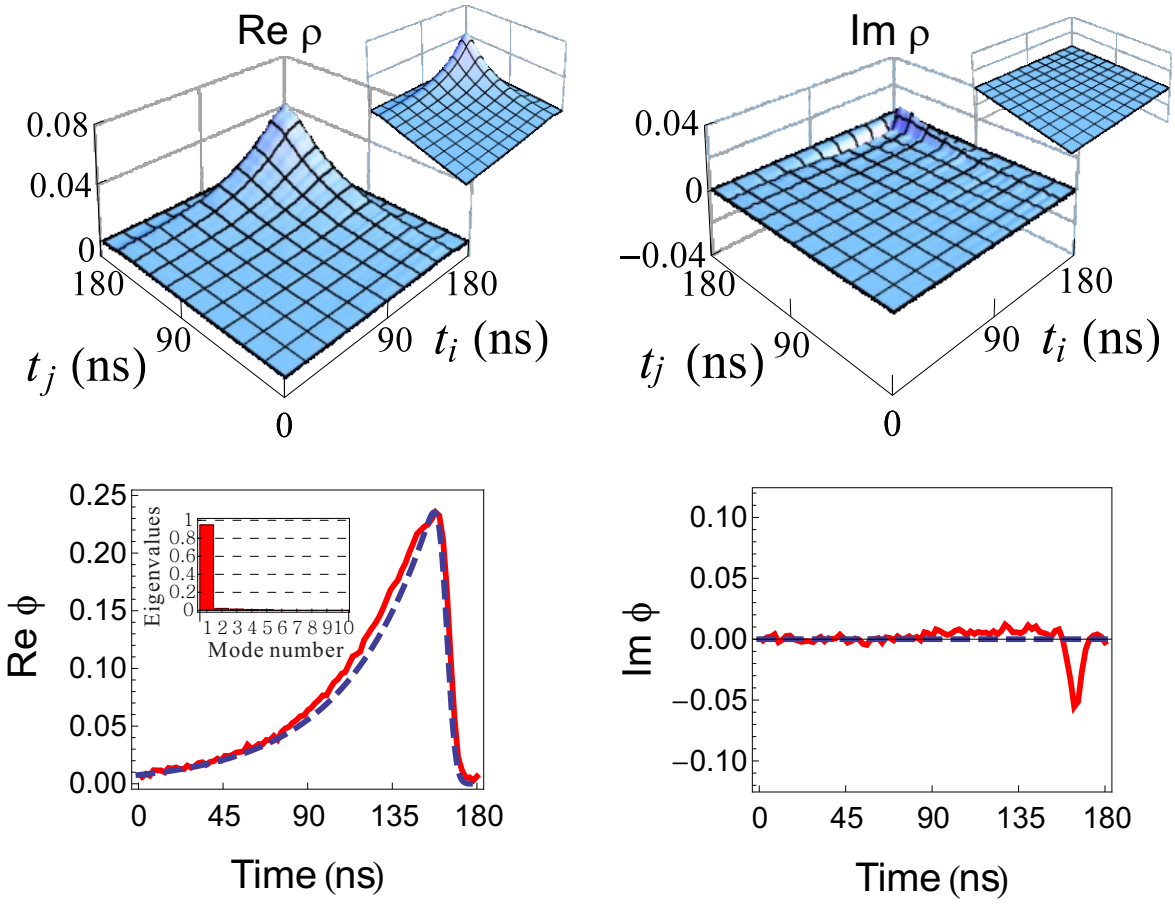

Figure 4.3: Experimentally reconstructed real (left) and imaginary (right) TDM (top) and TMF(bottom) for an unmodulated photon. The insets for the TDM plots show the theoretically obtained TDM for comparison. The insets in the bottom left figure show the distribution of eigenvalues from the experimentally calculated TDM. The red solid line represents the experimentally obtained TMF and the dashed blue lines represent the theoretical results. The trigger event occurs at $t = 155\ ns$.

4.3.2 For phase modulated photon

To illustrate the ability of the experimental technique to reconstruct the TDM in the case of a mixed state. We phase modulate the signal photons at a frequency $\omega_m = 2\pi \times 20$ MHz, larger than the spectral width of C2. This is achieved by passing the idler photons through an electro-optic modulator (EOM), with its optical axis oriented along the photon's polarization [45]. This modifies the TMF given by Eq. (4.5) by incorporating an extra phase factor

$$\phi^{\mathrm{EOM}}(t, \theta_m) = \sqrt{\gamma} e^{\gamma t/2} e^{-i\beta \sin(w_m t + \theta_m)} \Theta(-t), \tag{4.6}$$

where $\beta = 1.1$ is the modulation index[2] and θ_m is the phase of the modulating voltage at the time when the idler photon is detected. The single photon in the temporal mode given by Eq. (4.6) can be obtained by using the expression 3.2 as

$$|\Phi\rangle \equiv |1\rangle_{\phi^{\mathrm{EOM}}} = \sum_{t_k} \sqrt{\gamma} e^{\gamma t_k/2} e^{i\beta \sin(w_m t_k + \theta_m)} \Theta(-t_k) \, |1_k\rangle \tag{4.7}$$

For the mode given by $\phi^{\mathrm{EOM}}(t, \theta_m)$ the TDM can then be obtained trivially as

$$\begin{aligned} \rho^{\mathrm{EOM}}_{t,t'} &= \left\langle 1_t \,\middle|\, \hat{\rho}^{\mathrm{EOM}} \,\middle|\, 1_{t'} \right\rangle \\ &= \langle 1_t \,|\, \Phi \rangle \, \langle \Phi | 1_{t'} \rangle \\ &= \phi^{\mathrm{EOM}}(t, \theta_m) [\phi^{\mathrm{EOM}}(t', \theta_m)]^* \end{aligned} \tag{4.8}$$

Because the idler photon detections occur at random times, θ_m is randomized, leading to the following non-pure TDM:

$$\begin{aligned} \rho^{\mathrm{EOM}}_{t,t'} &= \frac{1}{2\pi} \int_{-\pi}^{\pi} \phi^{\mathrm{EOM}}(t, \theta_m) [\phi^{\mathrm{EOM}}(t', \theta_m)]^* d\theta_m \\ &= \gamma e^{\frac{\gamma(t+t')}{2}} \Theta(-t) \Theta(-t') J_0 \left[2\beta \sin\left(\frac{\omega_m (t - t')}{2} \right) \right], \end{aligned} \tag{4.9}$$

where J_0 is the Bessel function of the first kind.

[2] This was obtained by finding out the best fit of most significant mode calculated from the theoretical TDM 4.9 and the most significant temporal mode from experimentally calculated TDM (see Fig. 4.4).

It must be noted that the temporal mode structure of a phase modulated photon with random initial phase as discussed here is non-pure as is also revealed by the eigenvalue distribution in Fig 4.4. Therefore, temporal mode of such a photon as such is an ill-defined term. It is actually a mixture of modes resulting in the TDM of such a photon (see Eq. (3.5)). We concern ourselves with the dominant mode which is the one which has the highest eigenvalue.

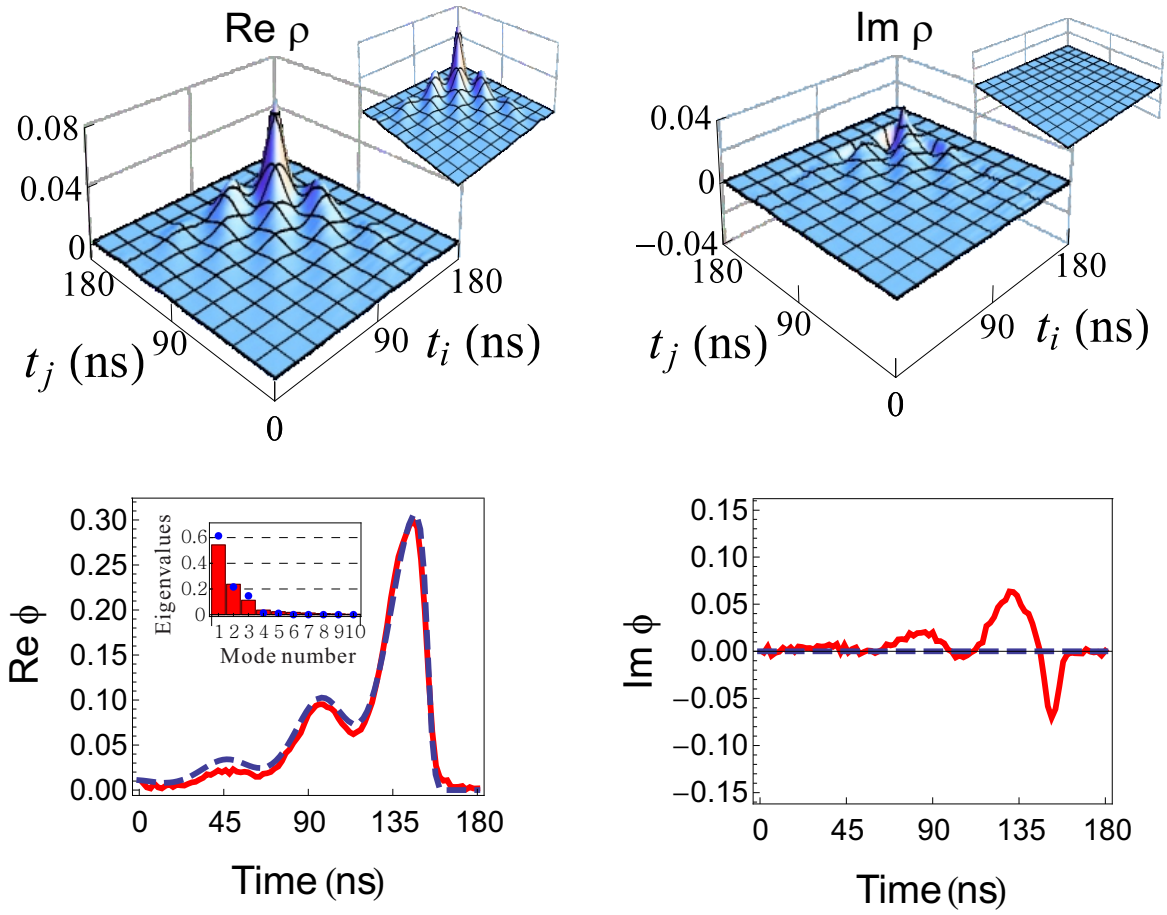

Figure 4.4: Experimentally reconstructed real (left) and imaginary (right), TDM (top) and most significant TMF (bottom), for an phase modulated photon. The insets for the TDM plots show the theoretically obtained TDM for comparison. The insets in the bottom left figure show the distribution of eigenvalues from the experimentally calculated TDM. The blue dots over the bars show the theoretically obtained eigenvalues. The red solid line represents the most significant TMF calculated from the experimental TDM and the dashed blue lines represent the theoretical results. The trigger event occurs at t = 155 ns

4.3.3 Virtual phase modulation

This is an extension of the last section in which we dealt with determining the temporal mode of an unmodulated and a phase modulated single photon. The mixed nature of phase

modulated photon in our case resulted in the imaginary part of the TDM going to zero. In this section we demonstrate the utility of our technique in the reconstruction of a temporal mode with a nonvanishing imaginary component. To this end, we induce a virtual phase modulation by redefining the signal-LO detuning according to $\delta\omega' = \delta\omega + \Delta$ when reconstructing the TDM from Eq. (3.14). The theoretically expected TMF and TDM can then be obtained as in section 4.3.1 by shifting the reference of ω_s by Δ, giving following results:

$$\phi^{\text{shifted}}(t) = \phi(t)e^{i\Delta t}; \tag{4.10}$$

$$\rho^{\text{shifted}}(t,t') = \rho(t,t')e^{i\Delta(t-t')}. \tag{4.11}$$

The TDM reconstructed from the experimental data using the effective modulation frequency of $\Delta = 2\pi \times 5$ MHz is shown in Fig. 4.5. While the purity of the temporal mode is maintained (shown by the dominant eigenvalue being ~ 1, see inset of Re[ϕ] Fig 4.5), the reconstructed density matrix now has a significant imaginary component, demonstrating the ability of our technique to accurately reconstruct states with complex temporal modes.

4.4 Other results

From the reconstructed TDMs we can calculate the fidelity with which our technique characterizes the temporal mode of the single photons with respect to the theoretical temporal profile. The fidelity would be defined in our case as

$$\mathcal{F} = \text{Tr}\left[\sqrt{\sqrt{\hat{\rho}_{exp}}\ \hat{\rho}_{th}\sqrt{\hat{\rho}_{exp}}}\right] \tag{4.12}$$

Substituting the obtained theoretical and experimental results we obtained the results as shown in Table 4.1.

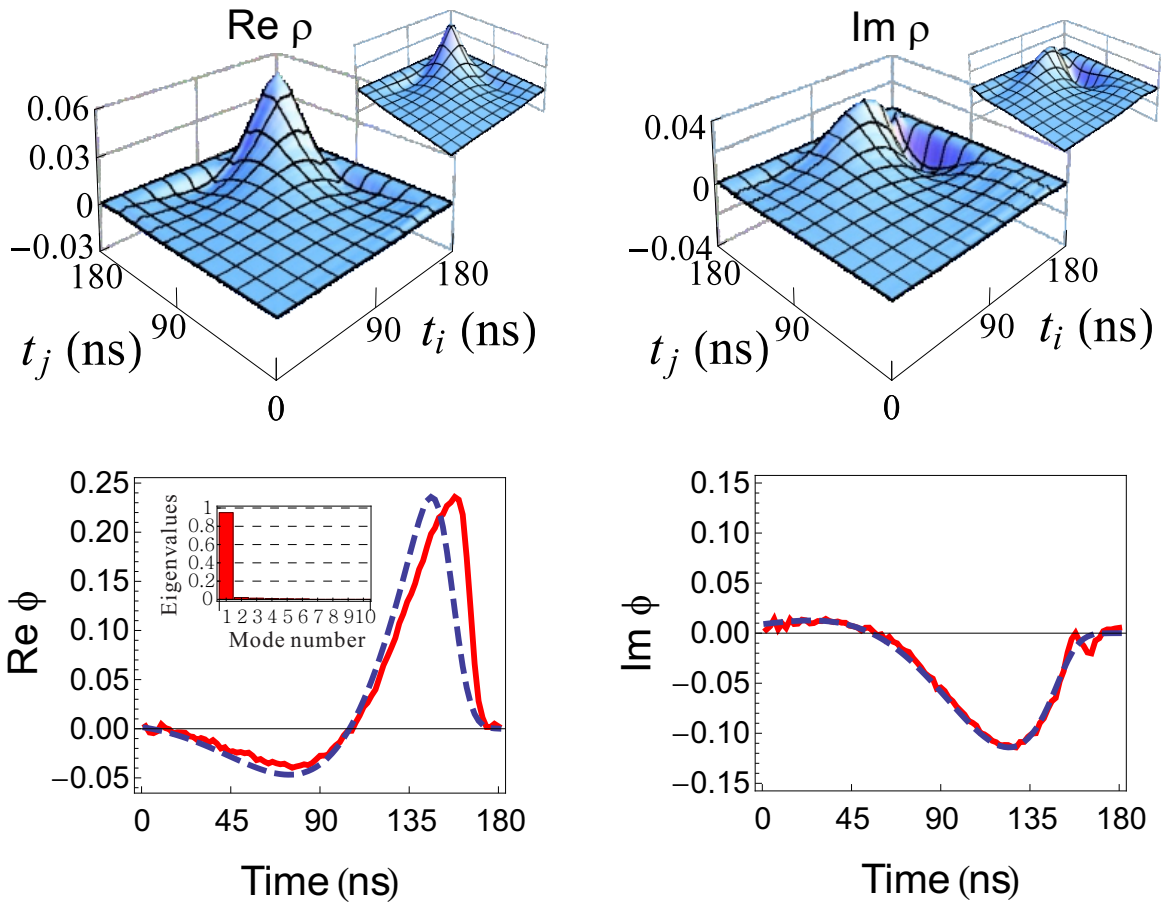

Figure 4.5: Experimentally reconstructed real (left) and imaginary (right) TDM (top) and TMF(bottom) for an virtually phase modulated photon. The insets for the TDM plots show the theoretically obtained TDM for comparison The insets in the bottom left figure show the distribution of eigenvalues from the experimentally calculated TDM. The red solid line represents the experimentally obtained TMF and the dashed blue lines represent the theoretical results. The trigger event occurs at $t = 155\ ns$.

Case	Fidelity
Unmodulated photon	0.97
Phase modulated photon	0.93
Virtual modulated photon	0.94

Table 4.1: Fidelity of reconstruction of the temporal density matrix in the three cases - unmodulated photon, phase modulated photon and virtual phase modulated photon.

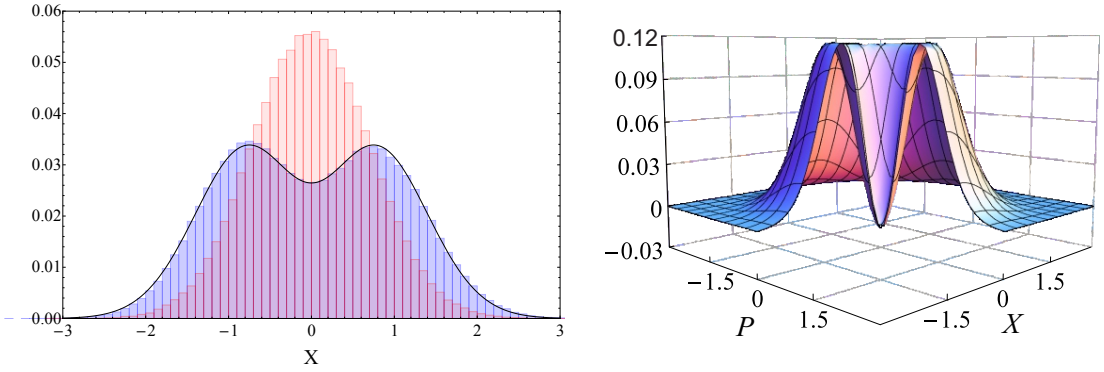

(a) Marginal distribution (b) Wigner function

Figure 4.6: (a) Experimental quadrature distribution (blue) overlaid with that for the vacuum state (red); (b) Wigner function corresponding to the Fock-basis density matrix for single photon generated by FWM.

The high fidelity of reconstruction demonstrates the robustness of our technique to characterize any arbitrary temporal mode structure of a photon with high accuracy. The theoretical knowledge of temporal mode is not needed for our technique to work. We just use it to compare the results obtained with our technique with the actual results.

From the reconstructed TMF for the unmodulated single photon, we can now reconstruct the Fock-basis density matrix for our single photon generated by FWM. We calculate the quadrature corresponding by integrating each homodyne photocurrent trace with TMF distribution obtained form the experimental results for the unmodulated photon. We use these quadratures to reconstruct the Fock-basis density matrix using the technique of iterative maximum-likelihood algorithm [46, 47]. The density matrix was found out to be

$$\hat{\rho} = \begin{pmatrix} 0.463 & 0 & 0 & 0 \\ 0 & 0.525 & 0 & 0 \\ 0 & 0 & 0.012 & 0 \\ 0 & 0 & 0 & 0 \end{pmatrix} \tag{4.13}$$

The Wigner function and the marginal distribution for the single photon state represented by 4.13 is shown in Fig 4.6.

Chapter 5

Conclusion

In this thesis, I have developed and experimentally demonstrated our technique of *polychromatic optical heterodyne tomography*, a robust method for experimental determination of temporal properties of a single photon directly from the time-resolved photocurrent statistics of balanced homodyne measurements. Our technique finds out the complete temporal density matrix of a single photon in the time domain. This enables us to extract the information about its temporal mode structure including any complex phase information or any multi-frequency components, the former being explicitly demonstrated in Section 4.3.3. Another important feature of our technique is that it can be used for characterizing non-pure (or mixed) modes as well, as demonstrated for the phase modulated photon in section 4.3.2. Furthermore, with a well defined modal structure for a pure single photon state, we were able to obtain a better measure of efficiency than by previous technique [38] using only an approximate guess temporal mode. This is an *in-situ* demonstration of the importance of knowing the correct temporal mode structure of a single photon in any quantum optical protocol as was motivated in Chapter 2. In general, accurate detection of the temporal mode is key for the proper mode matching required by many quantum communication protocols, and enables high efficiency tomographic reconstruction of the quantum optical state in the channel of interest.

Several improvements could be made to the experimental apparatus to implement this technique better. A very important improvement would be development of a broadband homodyne detector. In our case, the bandwidth of the homodyne detector was roughly twice as much as the bandwidth of the bi-photons generated by the process of FWM in ^{85}Rb vapor. Such a limited bandwidth of the homodyne detector leads to timing jitter which

is significant compared to the temporal width of the generated photon. As an effect, the observed temporal mode of the photon is distorted leading to inefficiencies in reconstruction of the state of the photon [33]. To eliminate this loss, we make our photons time-resolvable by homodyne measurements by means of tight-spectral filtering using a narrowband Fabry Perot cavity (transmission spectrum shown in Fig 3.2). However, we still suffered because of reduced count rate and of the inherent instability of the cavity resonance frequency over a period of time.

Another challenge which we faced in our demonstration was to model a phase modulated photon as discussed in section 4.3.2. At first it was not very clear why a model for phase modulated photon did not give matching theoretical results. But upon incorporating a random phase term corresponding to the phase of the modulated photon we obtained the correct theoretical model which corresponded to the observed results. This mixed nature of the temporal mode as a result of randomized phase could have been avoided if we could record the phase of the applied voltage on the EOM at the instant of the trigger. From this we can have a precise knowledge about the phase of the photon at the instant of detection. Collecting a large number of data sets for each phase could then be used to determine the temporal mode given by Eq. (4.6)at the cost of very low count rate for each phase. The nature of a phase modulated photon however is inherently mixed, in terms of its modal structure and our technique brings out its mixedness with a high fidelity. Moreover, the ability of our technique to determine any phase information in the TMF without losing the purity of the mode has clearly been demonstrated in section 4.3.3 where we induced a virtual phase modulation in the temporal mode of the photon and could determine both the real and imaginary components of the TMF and the TDM.

The ability to temporally characterize single photons with unknown arbitrary modal composition, pure or non-pure, has been demonstrated for the first time in this work. The major applications of POHT would be in the quantum memory based research community

where knowing the temporal structure of the photon with respect to the quantum memory temporal bandwidth is key to achieving a high efficiency. As shown, this method also has applications in characterizing single photon sources like ours with a much higher accuracy than before. Future extension to this work could be to develop a technique which could characterize temporal mode structure of higher order Fock states and other complicated derivatives of quantum optical states of light. I personally enjoyed working on this project and look forward to applying this technique to my future research endeavors.

Appendix A

Autocorrelation and Reduced Autocorrelation (Raw data)

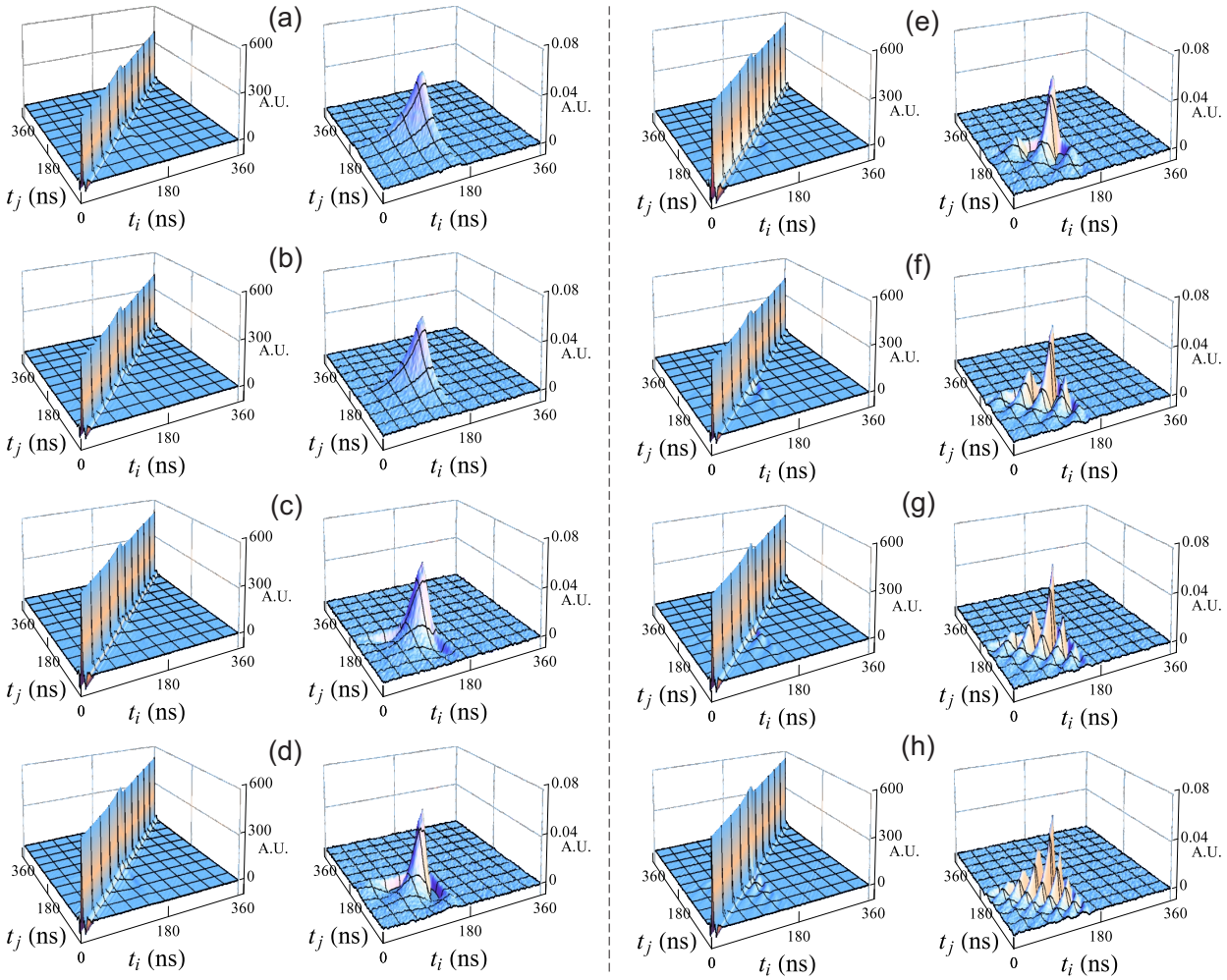

Figure A.1: Autocorrelation (left) and reduced autocorrelation (right) for the case of unmodulated photon. LO detuning (*a to h*): 0 MHz, 1.8 MHz, -5.1 MHz, 7.2 MHz, -10.8 MHz, 16.2 MHz, 19.2 MHz and 27 MHz. The trigger event occurs at $t = 155ns$. A.U. stand for arbitrary units. The reduced autocorrelation matrix is normalized.

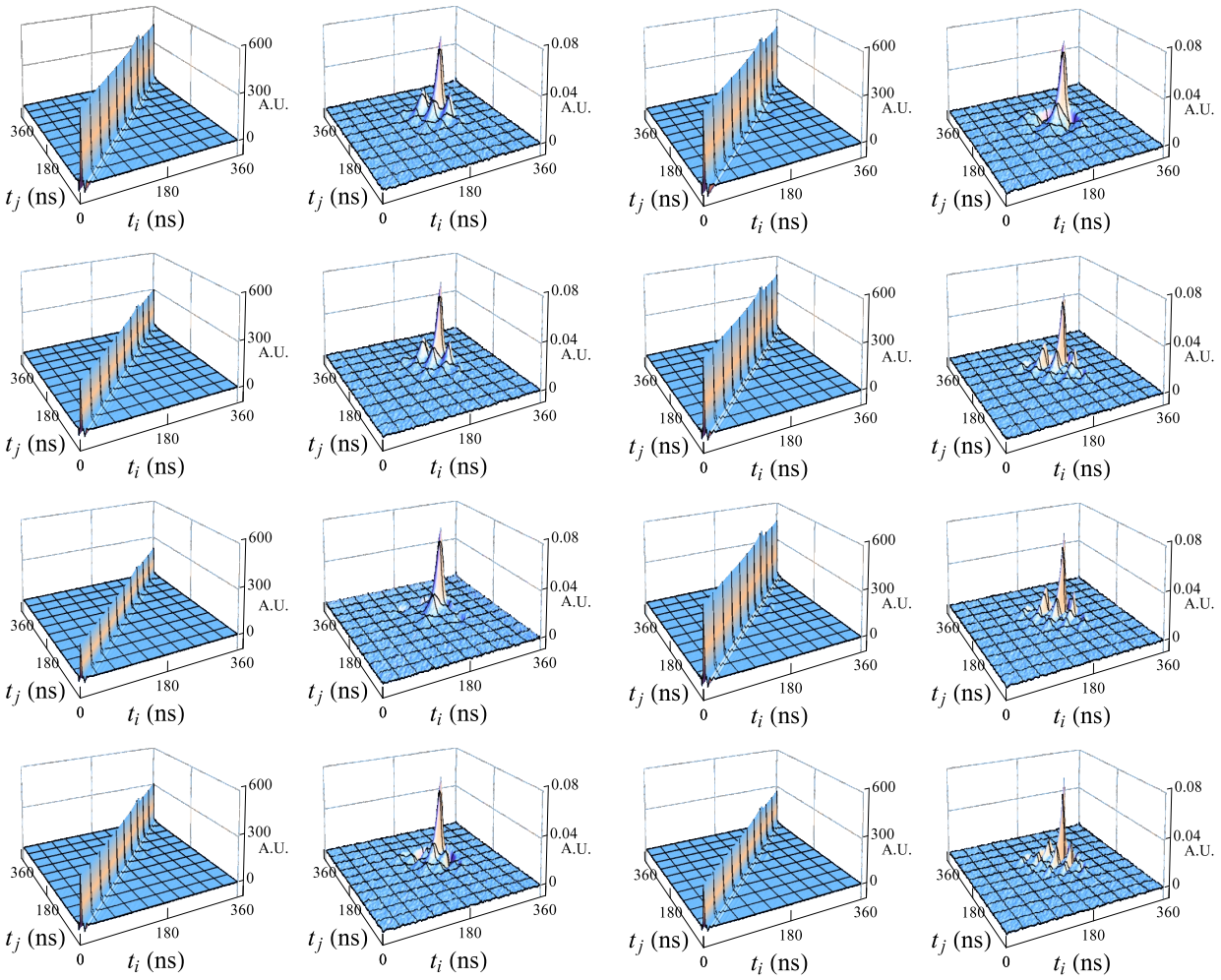

Figure A.2: Autocorrelation (left) and reduced autocorrelation (right) for the case of phase modulated photon. LO detuning (*a to h*): 0 MHz, 1.8 MHz, -5.1 MHz, 7.2 MHz, -10.8 MHz, 16.2 MHz, 19.2 MHz and 27 MHz. The trigger event occurs at $t = 255ns$. A.U. stand for arbitrary units. The reduced autocorrelation matrix is normalized.

Bibliography

[1] Daniel A Steck. Rubidium 85 d line data (2008).

[2] Nicolas Gisin, Grégoire Ribordy, Wolfgang Tittel, and Hugo Zbinden. Quantum cryptography. *Rev. Mod. Phys.*, 74:145–195, Mar 2002.

[3] Dik Bouwmeester, Jian-Wei Pan, Klaus Mattle, Manfred Eibl, Harald Weinfurter, and Anton Zeilinger. Experimental quantum teleportation. *Nature*, 390(6660):575–579, 1997.

[4] L-M Duan, MD Lukin, J Ignacio Cirac, and Peter Zoller. Long-distance quantum communication with atomic ensembles and linear optics. *Nature*, 414(6862):413–418, 2001.

[5] Emanuel Knill, Raymond Laflamme, and Gerald J Milburn. A scheme for efficient quantum computation with linear optics. *Nature*, 409(6816):46–52, 2001.

[6] Erwan Bimbard, Nitin Jain, Andrew MacRae, and AI Lvovsky. Quantum-optical state engineering up to the two-photon level. *Nat. Photon.*, 4(4):243–247, 2010.

[7] RE Slusher, LW Hollberg, Bernard Yurke, JC Mertz, and JF Valley. Observation of squeezed states generated by four-wave mixing in an optical cavity. *Phys. Rev. Lett.*, 55(22):2409, 1985.

[8] Itai Afek, Oron Ambar, and Yaron Silberberg. High-noon states by mixing quantum and classical light. *Science*, 328(5980):879–881, 2010.

[9] Paul G. Kwiat, Klaus Mattle, Harald Weinfurter, Anton Zeilinger, Alexander V. Sergienko, and Yanhua Shih. New high-intensity source of polarization-entangled photon pairs. *Phys. Rev. Lett.*, 75:4337–4341, Dec 1995.

[10] Vincent Boyer, AM Marino, and PD Lett. Generation of spatially broadband twin beams for quantum imaging. *Phys. Rev. Lett.*, 100(14):143601, 2008.

[11] Vincent Boyer, Alberto M Marino, Raphael C Pooser, and Paul D Lett. Entangled images from four-wave mixing. *Science*, 321(5888):544–547, 2008.

[12] Andrew M Weiner. Ultrafast optical pulse shaping: A tutorial review. *Opt. Commun.*, 284(15):3669–3692, 2011.

[13] Frédéric Grosshans and Philippe Grangier. Effective quantum efficiency in the pulsed homodyne detection of a n-photon state. *Eur. Phys. J. D*, 14(1):119–125, 2001.

[14] T Aichele, Alexander I Lvovsky, and S Schiller. Optical mode characterization of single photons prepared by means of conditional measurements on a biphoton state. *Eur. Phys. J. D*, 18(2):237–245, 2002.

[15] Magdalena Stobińska, Gernot Alber, and Gerd Leuchs. Perfect excitation of a matter qubit by a single photon in free space. *Europhys. Lett.*, 86(1):14007, 2009.

[16] Matthias Keller, Birgit Lange, Kazuhiro Hayasaka, Wolfgang Lange, and Herbert Walther. Continuous generation of single photons with controlled waveform in an ion-trap cavity system. *Nature*, 431(7012):1075–1078, 2004.

[17] J McKeever, A Boca, AD Boozer, R Miller, JR Buck, A Kuzmich, and HJ Kimble. Deterministic generation of single photons from one atom trapped in a cavity. *Science*, 303(5666):1992–1994, 2004.

[18] Ranjeet Kumar, Erick Barrios, Andrew MacRae, E Cairns, EH Huntington, and AI Lvovsky. Versatile wideband balanced detector for quantum optical homodyne tomography. *Opt. Comm.*, 285(24):5259–5267, 2012.

[19] Chonghoon Kim and Prem Kumar. Quadrature-squeezed light detection using a self-generated matched local oscillator. *Phys. Rev. Lett.*, 73:1605–1608, Sep 1994.

[20] J. S. Neergaard-Nielsen, B. Melholt Nielsen, C. Hettich, K. Mølmer, and E. S. Polzik. Generation of a superposition of odd photon number states for quantum information networks. *Phys. Rev. Lett.*, 97:083604, Aug 2006.

[21] Alexander I Lvovsky and Michael G Raymer. Continuous-variable optical quantum-state tomography. *Rev. Mod. Phys.*, 81(1):299, 2009.

[22] Jeff S Lundeen, Brandon Sutherland, Aabid Patel, Corey Stewart, and Charles Bamber. Direct measurement of the quantum wavefunction. *Nature*, 474(7350):188–191, 2011.

[23] BX Yang, WE Norum, S Shoaf, and J Stevens. Bunch-by-bunch diagnostics at the aps using time-correlated single-photon counting techniques. In *Proc. BIW, Santa Fe*, page 238, 2010.

[24] C Polycarpou, K. N. Cassemiro, G Venturi, A Zavatta, and M Bellini. Adaptive detection of arbitrarily shaped ultrashort quantum light states. *Phys. Rev. Lett.*, 109(5):053602, 2012.

[25] Olivier Morin, Claude Fabre, and Julien Laurat. Experimentally accessing the optimal temporal mode of traveling quantum light states. *Phys. Rev. Lett.*, 111(21):213602, 2013.

[26] Max Planck. On the law of distribution of energy in the normal spectrum. *Annalen der Physik*, 4(553):1, 1901.

[27] Paul AM Dirac. The quantum theory of the emission and absorption of radiation. In *Proc. Royal Soc. London, Series A*, volume 114, page 243, 1927.

[28] Herbert Goldstein. *Classical mechanics*, volume 4. Pearson Education India, 1962.

[29] Marlan O Scully. *Quantum optics*. Cambridge university press, 1997.

[30] Robert W Boyd. *Nonlinear optics*. Academic press, 2003.

[31] P. G. Kwiat, S. Barraza-Lopez, A. Stefanov, and N. Gisin. Experimental entanglement distillation and hidden non-locality. *Nature*, 409(6823):1014–1017, 2001.

[32] Vincent Boyer, Alberto M Marino, Raphael C Pooser, and Paul D Lett. Entangled images from four-wave mixing. *Science*, 321(5888):544–547, 2008.

[33] Travis Brannan, Zhongzhong Qin, Andrew MacRae, and AI Lvovsky. Generation and tomography of arbitrary qubit states in a transient collective atomic excitation. *arXiv preprint arXiv:1403.3463*, 2014.

[34] Leonard Mandel and Emil Wolf. *Optical coherence and quantum optics*. Cambridge university press, 1995.

[35] Christopher J Foot. *Atomic physics*. Oxford University Press, 2004.

[36] Ulf Leonhardt. Measuring the quantum state of light. *Measuring the Quantum State of Light, by Ulf Leonhardt, Cambridge, UK: Cambridge University Press, 2005*, 1, 2005.

[37] MV Fedorov, MA Efremov, AE Kazakov, KW Chan, CK Law, and JH Eberly. Spontaneous emission of a photon: Wave-packet structures and atom-photon entanglement. *Physical Review A*, 72(3):032110, 2005.

[38] A MacRae, T Brannan, R Achal, and A. I. Lvovsky. Tomography of a high-purity narrowband photon from a transient atomic collective excitation. *Phys. Rev. Lett.*, 109(3):033601, 2012.

[39] Pantita Palittapongarnpim, Andrew MacRae, and AI Lvovsky. Note: A monolithic filter cavity for experiments in quantum optics. *Rev. Sci. Instrum.*, 83(6):066101, 2012.

[40] Jürgen Appel, Andrew MacRae, and AI Lvovsky. A versatile digital ghz phase lock for external cavity diode lasers. *Meas. Sci. Technol.*, 20(5):055302, 2009.

[41] RE Scholten. Enhanced laser shutter using a hard disk drive rotary voice-coil actuator. *Review of scientific instruments*, 78(2):026101, 2007.

[42] Andrew MacRae. *An Atomic Source of Quantum Light*. PhD thesis, University of Calgary, 2012.

[43] Christopher Gerry and Peter Knight. *Introductory quantum optics*. Cambridge university press, 2005.

[44] Marianne Bader, Simon Heugel, Alexander L Chekhov, Markus Sondermann, and Gerd Leuchs. Efficient coupling to an optical resonator by exploiting time-reversal symmetry. *New J. Phys.*, 15(12):123008, 2013.

[45] Pavel Kolchin, Chinmay Belthangady, Shengwang Du, G. Y. Yin, and S. E. Harris. Electro-optic modulation of single photons. *Phys. Rev. Lett.*, 101:103601, Sep 2008.

[46] AI Lvovsky. Iterative maximum-likelihood reconstruction in quantum homodyne tomography. *Journal of Optics B: Quantum and Semiclassical Optics*, 6(6):S556, 2004.

[47] Jaroslav Řeháček, Zdeněk Hradil, E Knill, and AI Lvovsky. Diluted maximum-likelihood algorithm for quantum tomography. *Physical Review A*, 75(4):042108, 2007.